

Thermalization and dynamics in the single impurity Anderson model

Ireneusz Weymann,^{1,2,*} Jan von Delft,¹ and Andreas Weichselbaum¹

¹*Physics Department, Arnold Sommerfeld Center for Theoretical Physics and Center for NanoScience, Ludwig-Maximilians-Universität, Theresienstrasse 37, 80333 Munich, Germany*

²*Faculty of Physics, Adam Mickiewicz University, 61-614 Poznań, Poland*

(Dated: June 9, 2021)

We analyze the process of thermalization, dynamics and the eigenstate thermalization hypothesis (ETH) for the single impurity Anderson model, focusing on the Kondo regime. For this we construct the complete eigenbasis of the Hamiltonian using the numerical renormalization group (NRG) method in the language of the matrix product states. It is a peculiarity of the NRG that while the Wilson chain is supposed to describe a macroscopic bath, very few single particle excitations already suffice to essentially thermalize the impurity system at finite temperature, which amounts to having added a macroscopic amount of energy. Thus given an initial state of the system such as the ground state together with microscopic excitations, we calculate the spectral function of the quantum impurity using the microcanonical and diagonal ensembles. These spectral functions are compared to the time-averaged spectral function obtained by time-evolving the initial state according to the full Hamiltonian, and to the spectral function calculated using the thermal density matrix. By adding or removing particles at a certain Wilson energy shell on top of the ground state, we find qualitative agreement between the resulting spectral functions calculated for different ensembles. This indicates that the system thermalizes in the long-time limit, and can be described by an appropriate statistical-mechanical ensemble. Moreover, by calculating static quantities such as the impurity spectral density at the Fermi level as well as the dot occupancy for energy eigenstates relevant for microcanonical ensemble, we find good support for ETH. The ultimate mechanism responsible for this effective thermalization within the NRG can be identified as Anderson orthogonality: the more charge that needs to flow to or from infinity after applying a local excitation within the Wilson chain, the more the system looks thermal afterwards at an increased temperature. For the same reason, however, thermalization fails if charge rearrangement after the excitation remains mostly local. In these cases, the different statistical ensembles lead to different results. Their behavior needs to be understood as a plain microscopic quantum quench only.

PACS numbers: 72.15.Qm, 05.30.-d, 73.63.Kv

I. INTRODUCTION

In an isolated many-body quantum system, the dynamics can drive the system towards a stationary state that resembles a thermal state.^{1,2} Its resulting macroscopic properties are therefore consistent with statistical mechanics.^{3,4} Thermalization exhibits a certain universality, in that widely different initial conditions can lead to very similar thermal states.⁵⁻⁷ Several recent studies have aimed at finding the reason for this universality.⁷⁻¹³ It has been argued that for generic isolated interacting quantum systems the process of thermalization is described by eigenstate thermalization hypothesis (ETH).^{5,6} ETH states that expectation values of generic observables calculated using a *diagonal* ensemble derived from a single generic many-body state and characterized by a density matrix that is diagonal in energy eigenbasis, and those calculated for a proper energy eigenstate, are equal. This happens if eigenstates that are close in energy yield similar expectation values for the operator in question. It implies that the knowledge of a single eigenstate with energy falling within a proper energy window is sufficient to describe the system in its thermal state. Although for systems displaying *simple* correlations the ETH may be rather intuitive,⁷ it is definitely not obvious for fully-interacting many-body

problems, the description of which involves exponentially large Hilbert spaces.

In this paper we study the process of thermalization and explore the applicability of the ETH for a particular interacting many-body system, namely the single-impurity Anderson model (SIAM). For this model, a complete basis of approximate eigenstates of the Hamiltonian can be constructed using the numerical renormalization group (NRG) method.^{14,15} The availability of this complete basis of energy eigenstates allows numerous aspects of the ETH to be analyzed in great detail.

The SIAM describes a localized electronic level (the *quantum impurity*, henceforth called quantum dot) with local interactions, that hybridizes with a band of conduction electrons. Proposed originally to explain the formation of local moments in metals,¹⁶ this model and generalizations thereof have been commonly used to model transport through small quantum dots coupled to leads.¹⁷⁻¹⁹ When the local level, henceforth called dot level, has average occupancy $n_{d\sigma} = \langle \hat{d}_\sigma^\dagger \hat{d}_\sigma \rangle \simeq \frac{1}{2}$ per spin species, it hosts a localized spin which experiences exchange interactions with the spins of the conduction band, leading to the Kondo effect.^{20,21} At temperatures below the Kondo temperature, T_K , the conduction electrons screen the dot's spin, forming a nonlocal singlet state.^{20,21} The many-body correlations involved in this

screening can be characterized²¹ in terms of the local density of states (LDOS). For the ground state $|\mathcal{G}\rangle$, the LDOS is given by the local spectral function, defined as the expectation value $A_{\mathcal{G}} = \langle \mathcal{G} | \hat{\mathcal{A}} | \mathcal{G} \rangle$ of the spectral operator $\hat{\mathcal{A}} \equiv \sum_{\sigma} (\hat{\mathcal{A}}_{\sigma}^{+} + \hat{\mathcal{A}}_{\sigma}^{-})$, where

$$\begin{aligned} \hat{\mathcal{A}}_{\sigma}^{+} &= \hat{d}_{\sigma} \delta(\omega - \hat{H} + E_0) \hat{d}_{\sigma}^{\dagger} \\ \hat{\mathcal{A}}_{\sigma}^{-} &= \hat{d}_{\sigma}^{\dagger} \delta(\omega + \hat{H} - E_0) \hat{d}_{\sigma}, \end{aligned} \quad (1)$$

with $\delta(\omega)$ the Dirac delta function, \hat{H} the Hamiltonian, and E_0 the ground state energy. The spectral operator $\hat{\mathcal{A}}$ measures the likelihood of raising or lowering the energy by ω upon adding or removing an electron from the dot. When $A_{\mathcal{G}}$ is viewed as function of ω (implicit in our notation) the ground state spectral function exhibits a striking, sharp peak near the Fermi level, the so-called Kondo-Abrikosov-Suhl resonance,²¹ whose width is a measure of the Kondo temperature, T_K . This resonance is characteristic for the spectral function

$$A_{\Psi} = \langle \Psi | \hat{\mathcal{A}} | \Psi \rangle \quad (2)$$

of any quantum state $|\Psi\rangle$ for which the average energy and energy uncertainty,

$$E_{\Psi} = \langle \Psi | \hat{H} - E_0 | \Psi \rangle \quad (3a)$$

$$\Delta E_{\Psi} = \sqrt{\langle \Psi | (\hat{H} - E_0)^2 | \Psi \rangle - E_{\Psi}^2} \quad (3b)$$

both lie below the Kondo temperature (meaning the energy of the system when $T = T_K$). However, the resonance weakens and eventually disappears once E_{Ψ} and/or ΔE_{Ψ} becomes larger than T_K (examples are shown below). As a result, the Kondo resonance causes a striking enhancement in the transmission through the dot if the temperature and source-drain bias are lowered to become smaller than T_K , causing a zero-bias anomaly that has been observed in numerous experiments.²²⁻²⁴

An accurate description of Kondo correlations in general and the LDOS in particular requires sophisticated theoretical tools. In this regard, the NRG has proven itself to be a particularly powerful and versatile method for studying various quantum impurity models.^{14,15} NRG employs a logarithmic discretization of the conduction band and maps the model onto a tight-binding chain with exponentially decaying hoppings, $t_n \sim \Lambda^{-n/2}$ with dimensionless discretization parameter $\Lambda \gtrsim 2$, the so-called Wilson chain. This chain is diagonalized iteratively by adding one site at a time,¹⁴ and the eigenstates calculated during this iterative scheme^{25,26} can be used to construct a complete many-body basis of approximate eigenstates of the Hamiltonian, the Anders-Schiller (AS) basis.^{25,26} Using the AS-basis, it is possible to accurately calculate spectral functions of local operators^{27,28} and in particular to reliably determine the shape of the Kondo resonance. Moreover, the time evolution $|\Psi_t\rangle$ of an arbitrary initial quantum state $|\Psi\rangle$ can be calculated by representing the latter in the AS-basis.^{25,26} With this approach, called time-dependent NRG (tNRG), it is possible to explicitly

calculate the evolution of operator expectation values, such as that of the spectral operator $\hat{\mathcal{A}}$.

Since tNRG treats the entire many-body Hilbert space as a closed quantum system when calculating the time-evolution $|\Psi_t\rangle$, it is ideally suited to studying thermalization and the ETH for interacting many-body systems. In this paper, we do this for the SIAM. We consider a variety of initial states $|\Psi\rangle$, some correlated, some not, explore how Kondo correlations emerge in the long-time limit, and analyze to what extent the results correspond to those expected for a thermal state. We will use the time-dependent expectation value of the spectral operator,

$$A_t = \langle \Psi_t | \hat{\mathcal{A}} | \Psi_t \rangle, \quad (4)$$

as diagnostic tool for the emergence of Kondo correlations with time: they lead to the emergence of a Kondo resonance in A_t , when viewed as function of ω for a series of fixed but ever larger values of t . Moreover, the width of the Kondo resonance in A_t for $t \rightarrow \infty$ can serve as a measure of the effective temperature of the system in the long-time limit as long as this width is larger than T_K . Note, however, that the simultaneous t and ω -dependence of A_t will presumably not be accessible experimentally; thus, A_t is to be regarded mainly as a useful diagnostic tool for theoretical analysis.

To study the dynamics of the system and assess the applicability of ETH, we compare the long-time limit of the LDOS to the LDOS calculated within three different ensembles: (i) diagonal ensemble which is characterized by a density matrix that is diagonal in the energy eigenbasis; (ii) the microcanonical ensemble corresponding to a fixed energy, E_{Ψ} , cf. Eq. (3); and (iii) the standard thermal grand canonical ensemble²⁷ at comparable temperature $T \sim E_{\Psi}$. We study the process of thermalization for the ground state and a few excited states, where the excitations are created either in the bath or at the impurity. More specifically, we consider the states which are created by acting with a single-particle operator or a density operator on the full many-body ground state of the system. We also analyze the dynamics and long-time behavior of the system for an initial state in which the dot is decoupled from the leads, and for a state with single-particle excitation in the dot. We show that when starting the time evolution with a state for which the excitation was created within the Wilson chain by adding or removing charge, we get a local density of states that is similar to that obtained with a microcanonical ensemble of corresponding energy. By calculating the expectation values of the spectral function at the Fermi level and the dot occupancy for energy eigenstates relevant for the microcanonical ensemble, we demonstrate that, indeed, thermalization occurs and that ETH applies. However, a rather different behavior is observed for states that only involve local rearrangement of any of the conserved charges. We show that here the time evolution needs to be interpreted as a microscopic quantum quench that occurs on top of a given initial statistical ensemble.

The paper is organized as follows. In Sec. II we describe the general concept of the ETH, the model and Hamiltonian, as well as the different ensembles used to study the dynamics of the system. Section III is devoted to testing the process of thermalization and the ETH for different initial states. The conclusions are given in Sec. IV, while the details of the construction of respective statistical ensembles using the NRG eigenbasis are presented in the Appendix.

II. THEORETICAL DESCRIPTION

A. General statement of ETH

Consider a generic isolated quantum system with Hamiltonian \hat{H} , with its complete many-body eigenbasis given by $|s\rangle$, i.e. $\hat{H}|s\rangle = E_s|s\rangle$. Suppose the system is initialized at time $t=0$ in a pure quantum state, $|\Psi\rangle = \sum_s C_s|s\rangle$, with $C_s = \langle s|\psi\rangle$. To what extent does the expectation value of an observable \hat{O} ,

$$O_t = \langle \Psi_t | \hat{O} | \Psi_t \rangle, \quad (5)$$

with $|\Psi_t\rangle \equiv e^{-i\hat{H}t}|\Psi\rangle$, depend on the initial state $|\Psi\rangle$ in the long-time limit, $t \rightarrow \infty$?

Since the system is closed, quantum mechanics gives the answer

$$O_\infty = \sum_s |C_s|^2 \mathcal{O}_{ss}, \quad (6)$$

where $\mathcal{O}_{ss'} \equiv \langle s | \hat{O} | s' \rangle$, which assumes that the contribution of the off-diagonal matrix elements averages to zero due to phase cancellations, i.e. $\lim_{t \rightarrow \infty} \sum_{s \neq s'} e^{i(E_s - E_{s'})t} \mathcal{O}_{ss'} = 0$. Thus, the long-time limit is described by a diagonal ensemble, characterized by a density matrix that is diagonal in the energy eigenbasis,

$$O_{\text{diag}} = \text{Tr}[\hat{\rho}_{\text{diag}} \hat{O}] \quad (7a)$$

$$\text{with } \hat{\rho}_{\text{diag}} \equiv \sum_s |C_s|^2 \hat{P}_s, \quad (7b)$$

where $\hat{P}_s \equiv |s\rangle\langle s|$ is the projector onto eigenstate $|s\rangle$.

However, standard statistical mechanics gives a different answer: it assumes that the long-time limit is well described by a microcanonical ensemble,

$$O_{\text{micro}} = \text{Tr}[\hat{\rho}_{\text{micro}} \hat{O}] \quad (8a)$$

$$\text{with } \hat{\rho}_{\text{micro}} \equiv \frac{1}{N_\Psi} \sum_{|E_s - E_\Psi| \leq \delta E_\Psi} \hat{P}_s, \quad (8b)$$

characterized by the initial state's average energy E_Ψ and a (narrow) energy window $\delta E_\Psi \ll \Delta E_\Psi$ [cf. Eq. (3)], with N_Ψ the number of states in the energy window that is being summed over. The system is said to behave thermally if in the long-time limit the expectation

values calculated using diagonal and microcanonical ensembles are equal, i.e. $O_{\text{diag}} = O_{\text{micro}}$. One possible scenario for which this occurs, discussed by Deutsch and Srednicki,^{5,6} is the eigenstate thermalization hypothesis, which assumes that the eigenstate expectation values \mathcal{O}_{ss} show only very weak state-to-state fluctuations for states that are close in energy. If this is the case, the knowledge of the expectation value \mathcal{O}_{ss} of observable \mathcal{O} for a *single* eigenstate with appropriately chosen energy is sufficient to describe the system's behavior in the long time limit.

Given the difference in form between Eqs. (7) and (8), the intriguing question arises: under what conditions are the two equivalent? Does the eigenstate thermalization hypothesis also hold for truly interacting, nontrivial many-body systems? The main goal of this paper is to address these questions for the single impurity Anderson Hamiltonian.

B. Model Hamiltonian and NRG basics

1. Model Hamiltonian

The SIAM describes a single-level quantum dot that is tunnel-coupled to a conduction band of free electrons. Its Hamiltonian takes the form¹⁶

$$\hat{H} = \hat{H}_{\text{lead}} + \underbrace{\hat{H}_{\text{dot}} + \hat{H}_{\text{tun}}}_{\equiv \hat{H}_{\text{loc}}}, \quad (9a)$$

where

$$\hat{H}_{\text{lead}} = \sum_{k\sigma} \varepsilon_k \hat{c}_{k\sigma}^\dagger \hat{c}_{k\sigma} \quad (9b)$$

$$\hat{H}_{\text{dot}} = \sum_{\sigma} \varepsilon_d \hat{d}_{\sigma}^\dagger \hat{d}_{\sigma} + U \hat{d}_{\uparrow}^\dagger \hat{d}_{\uparrow} \hat{d}_{\downarrow}^\dagger \hat{d}_{\downarrow} \quad (9c)$$

$$\hat{H}_{\text{tun}} = \sum_{k\sigma} v \left(\hat{c}_{k\sigma}^\dagger \hat{d}_{\sigma} + \hat{d}_{\sigma}^\dagger \hat{c}_{k\sigma} \right). \quad (9d)$$

\hat{H}_{lead} describes a band of noninteracting conduction electrons, where $\hat{c}_{k\sigma}^\dagger$ creates an electron with spin $\sigma \in \{\uparrow, \downarrow\}$ at energy ε_k . \hat{H}_{dot} describes a dot state with level energy ε_d , creation operator \hat{d}_{σ}^\dagger and local Coulomb energy U . \hat{H}_{tun} accounts for tunneling between the dot and the conduction band, with energy-independent hopping matrix element v . Therefore \hat{H}_{loc} accounts for the local part of the Hamiltonian that includes the quantum dot as well as the bath degrees of freedom at the location of the impurity.

If $n_{d\sigma} \simeq \frac{1}{2}$, the electronic correlations can lead to the Kondo effect at low temperatures, when due to spin-flip cotunneling processes the dot's spin becomes screened by the conduction electrons. To resolve the Kondo physics, we use NRG.^{14,15,25-27} There the total system Hamiltonian is described by $\hat{H} \equiv \lim_{N \rightarrow \infty} \hat{H}_N$ with

$$\hat{H}_N = \hat{H}_{\text{loc}} + \sum_{n=0}^{N-1} t_n \sum_{\sigma} \left(\hat{f}_{n\sigma}^\dagger \hat{f}_{n+1\sigma} + \text{H.c.} \right), \quad (10a)$$

such that $\hat{H}_0 \equiv \hat{H}_{\text{loc}}$, where

$$\hat{H}_{\text{loc}} = \hat{H}_{\text{dot}} + \sqrt{\frac{2\Gamma}{\pi}} \sum_{\sigma} \left(\hat{d}_{\sigma}^{\dagger} \hat{f}_{0\sigma} + \text{H.c.} \right). \quad (10b)$$

The operators $\hat{f}_{n\sigma}$ act on the n th shell of the Wilson chain, with t_n the respective nearest-neighbor hoppings along the chain. For simplicity, a constant hybridization strength $\Gamma(\omega) \equiv \Gamma \vartheta(D - |\omega|)$ is assumed, with level half-width $\Gamma \equiv \pi \rho |v|^2$ and half-bandwidth $D := 1$, taken as the unit of energy throughout. Similarly, units of time and temperature are fixed by using $\hbar = k_B = 1$, respectively.

2. Complete basis sets

The NRG Hamiltonian in Eq. (10) can be solved in an iterative way, by constructing and diagonalizing the Hamiltonian shell-wise. Due to exponentially growing Hilbert space with increasing the iteration number n , one needs to truncate the space by keeping only M_K lowest-energy states at a given iteration. Thus, each Wilson shell, up to the last iteration, $n = N$, contains the low-energy states retained for the next iteration, i. e. the kept (K) states, and the discarded (D) states (starting from shells, $n \geq n_0$, where n_0 is the iteration at which one first begins to truncate), while at the last shell (for $n = N$) all states are regarded as discarded. The discarded states can be used to define a complete eigenbasis of the Hamiltonian,

$$\mathbf{1} = \sum_{n \geq n_0}^N \sum_{se} |se\rangle_n^D \langle se|, \quad (11a)$$

which, to a good approximation due to presence of energy scale separation along the Wilson chain, also forms an eigenbasis of the full Hamiltonian,^{25,26}

$$\hat{H} |se\rangle_n^X \simeq E_{ns}^X |se\rangle_n^X. \quad (11b)$$

Here $|se\rangle_n^X$ denotes a kept or discarded ($X \in K, D$) state s on the Wilson chain at shell n , e is an index labeling environmental states describing the rest of the chain (shells with larger n), and E_{ns}^X is the corresponding approximate eigenenergy. Note that the discarded states are defined on the Wilson shells from $n = n_0$ to $n = N$. The states obtained by diagonalizing the NRG Hamiltonian can be conveniently expressed in terms of matrix product states (MPS),^{27,29} see Fig. 1. The coefficients of any state $|\Psi\rangle$ in this complete eigenbasis will be denoted by $C_{nse}^D \equiv \langle se | \Psi \rangle$.

3. Model parameters

We use the following parameters throughout this paper: $U = 0.12$, $\Gamma = 0.01$, and $\varepsilon_d = -U/3$. This yields

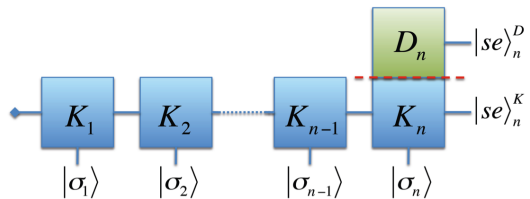


FIG. 1. (color online) Matrix product state (MPS) representation of the kept (K) and discarded (D) states on the Wilson chain. The n th box represents the tensor block X_n ($X \in \{K, D\}$), while its bottom, left and right legs carry the labels of the local states $|\sigma_n\rangle$, the kept states $|se\rangle_{n-1}^K$, and the kept (discarded) states $|se\rangle_n^K$ ($|se\rangle_n^D$), respectively.

the Kondo temperature,³⁰ $T_K \simeq 3.7 \times 10^{-4}$ (in units of $D = 1$). For the Wilson chain we take the following parameters: the discretization $\Lambda = 2$, the chain length $N = 50$, and we keep $M_K = 1024$ states for each iteration, unless stated otherwise. Moreover, in calculations we used the Abelian symmetry for the total charge and the total spin z -th component. Using the complete eigenbasis, we calculate the relevant matrix elements and collect the discrete spectral function data points in a dense logarithmic mesh. In order to represent the continuum model, this discrete data subsequently needs to be broadened. Here we follow the standard prescription^{15,27} of approximating the Dirac delta function by log-Gaussian distributions, while smoothly switching to a standard Gaussian distribution for $|\omega| < \omega_0$ in order to broaden across $\omega = 0$, with $\omega_0 = E_{\Psi}$, unless stated otherwise. The latter is required since the resolution of NRG below temperature – here more broadly the energy of the system – is intrinsically limited by energy scale separation.²⁷

C. Density matrices

Using the complete eigenbasis of the NRG Hamiltonian, it is possible to calculate the thermal grand canonical expectation value $O_{\text{grand}} = \text{Tr}[\hat{\rho}_{\text{grand}} \hat{O}]$ of any operator, with the grand canonical density matrix represented as²⁷

$$\begin{aligned} \hat{\rho}_{\text{grand}} &= \sum_n \sum_{se} |se\rangle_n^D \frac{e^{-\beta E_{ns}^D}}{Z} \langle se| \\ &\equiv \sum_n w_n^{\text{grand}} \hat{\rho}_n^{\text{grand}}, \end{aligned} \quad (12)$$

with the chemical potential set to zero, $\mu = 0$, and $\beta = 1/T$. Here $\hat{\rho}_n^{\text{grand}}$ is the density matrix of shell n within the state space $s \in D$, $w_n^{\text{grand}} = d^{N-n} Z_n / Z$ is the total weight of shell n , with the partition function Z_n and $d = 4$ the dimension of the local state space of a Wilson site. Henceforth, we use the abbreviated notation $\sum_n \equiv \sum_{n \geq n_0}^N$ for the sum over the Wilson shells with $n \geq n_0$. This notation will be used for all ensembles considered in this paper.

With the complete eigenbasis, the density matrices for the microcanonical and diagonal ensembles can also be constructed. Similarly to $\hat{\rho}_{\text{grand}}$, any of the ensembles \mathcal{E} has a decomposition over the Wilson shells of the general form

$$\hat{\rho}_{\mathcal{E}} = \sum_n w_n^{\mathcal{E}} \hat{\rho}_n^{\mathcal{E}}. \quad (13)$$

The NRG specific details of the implementation of the aforementioned ensembles can be found in App. A.

III. RESULTS AND DISCUSSION

In the following we study the dynamics of the system for various excitations on top of the ground state of the system. In particular, this includes single-particle excitation by adding or removing a particle using $|\Psi\rangle = \hat{f}_{n\sigma}^\dagger |\mathcal{G}\rangle$ (Sec. III A), density-like excitations such as $|\Psi\rangle = \hat{f}_{n\sigma}^\dagger \hat{f}_{n\sigma} |\mathcal{G}\rangle$ (Sec. III B), and quantum quenches in the hybridization of the impurity (Sec. III C). Here the order in which we discuss these cases is chosen such that displaced charge, i. e. charge that needs to flow to or from infinity, is maximal in the first case while it is smallest in the last case. Accordingly as will be shown below, thermalization and hence ETH is best satisfied in the first case, but not in the last.

The expectation value we are interested in is the full many-body spectral function $A_{\mathcal{E}}(\omega)$ of the dot level (local density of states, LDOS) for a specified ensemble \mathcal{E} , as this is most sensitive to correlations within the system. Here $A(\omega) = -\frac{1}{\pi} \sum_{\sigma} \text{Im} G_{d\sigma}^R(\omega)$, where $G_{d\sigma}^R(\omega)$ denotes the Fourier transform of the retarded Green's function, $G_{d\sigma}^R(\tau) = -i\theta(\tau) \langle \{ \hat{d}_{\sigma}(\tau), \hat{d}_{\sigma}^{\dagger}(0) \} \rangle_{\mathcal{E}}$. The spectral operator \hat{A} is defined by

$$\hat{A} = \frac{1}{\pi} \sum_{\sigma} \int_0^{\infty} d\tau \{ \hat{d}_{\sigma}(\tau), \hat{d}_{\sigma}^{\dagger}(0) \} e^{i\omega\tau}. \quad (14)$$

which for the ground state of the system yields Eq. (1). The corresponding spectral function is given by

$$A_{\mathcal{E}} = \text{Re}\{\text{Tr}[\hat{\rho}_{\mathcal{E}} \hat{A}]\}, \quad (15)$$

with the density matrix $\hat{\rho}_{\mathcal{E}}$ for a specific statistical ensemble \mathcal{E} given by Eq. (13), or for a single state $|\Psi_t\rangle$ by $\hat{\rho}_{\Psi_t} = |\Psi_t\rangle\langle\Psi_t|$.

Here three different ensembles have been analyzed: the grand canonical, the microcanonical and the diagonal ensemble. The spectral function for the grand canonical ensemble, A_{grand} , was calculated at an effective temperature T_{Ψ} , such that $E_{\Psi} = \text{Tr}[\hat{\rho}_{\text{grand}} \hat{H}]$, unless stated otherwise. As in Eq. (3), the energy E_{Ψ} was measured relative to the ground state energy E_0 throughout. The calculation of the spectral function for the diagonal and microcanonical ensembles using the respective density matrices can be performed in a way similar to the *full* density matrix calculations,²⁷ see App. A. Having generated the

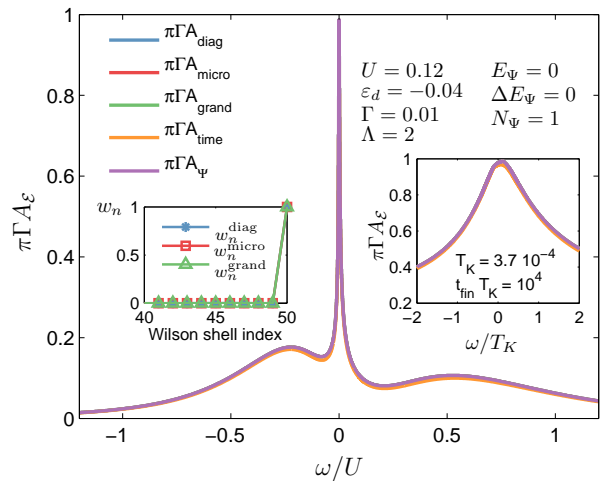


FIG. 2. (color online) The normalized spectral function $\pi\Gamma A_{\mathcal{E}}$ of the dot level at $T = 0$ calculated by using the diagonal ensemble A_{diag} , the microcanonical ensemble A_{micro} , the grand canonical ensemble A_{grand} , the time-evolved state in the long time limit A_{time} , as well as the spectral function A_{Ψ} calculated for the initial state $|\Psi\rangle = |\mathcal{G}\rangle$. The left inset displays the weights on the Wilson chain w_n for the diagonal (w_n^{diag}), microcanonical (w_n^{micro}) and grand canonical (w_n^{grand}) ensembles for fixed finite length $N = 50$, while the right inset represents a plain zoom of the spectral data around the Kondo peak.

eigenbasis of the NRG Hamiltonian in a forward sweep over the Wilson chain, a subsequent backward sweep is performed to determine the respective density matrices with corresponding weights. This basically enables the calculation of all relevant operator expectation values including, in particular, the expectation value of the spectral function operator \hat{A} .

Moreover, we have also calculated the spectral function for the initial state, $A_{\Psi} = \langle \Psi | \hat{A} | \Psi \rangle$, and for the time-evolved state in the long time limit,

$$A_{\text{time}} = \frac{1}{\delta t} \int_{t_{\text{fin}} - \delta t}^{t_{\text{fin}}} dt A_t, \quad (16)$$

where t_{fin} is the final time and δt is the time over which the averaging is performed. In calculations we use $t_{\text{fin}} T_K = 10^4$ and $\delta t = 0.2 t_{\text{fin}}$. The details of the calculation of time-averaged spectral function are presented in App. B.

To begin with and also for later reference, let us start with analyzing the behavior of the normalized spectral function $\pi\Gamma A_{\mathcal{G}}$ for the ground state of the system, i. e. $|\Psi\rangle = |\mathcal{G}\rangle$, where through Friedel-sum-rule, one expects $\pi\Gamma A(\omega = 0) \simeq 0.99$ (see Fig. 2). The spectral function displays two broad maxima at resonant energies $\omega = \varepsilon_d$ and $\omega = \varepsilon_d + U$, and a narrow Kondo resonance²¹ of width T_K pinned at the Fermi level $\omega = 0$.

The spectral functions shown in Fig. 2 are calculated by using the diagonal ensemble, A_{diag} , the microcanonical ensemble, A_{micro} , and grand canonical ensemble, A_{grand} . Because $|\Psi\rangle = |\mathcal{G}\rangle$ is an eigenstate of

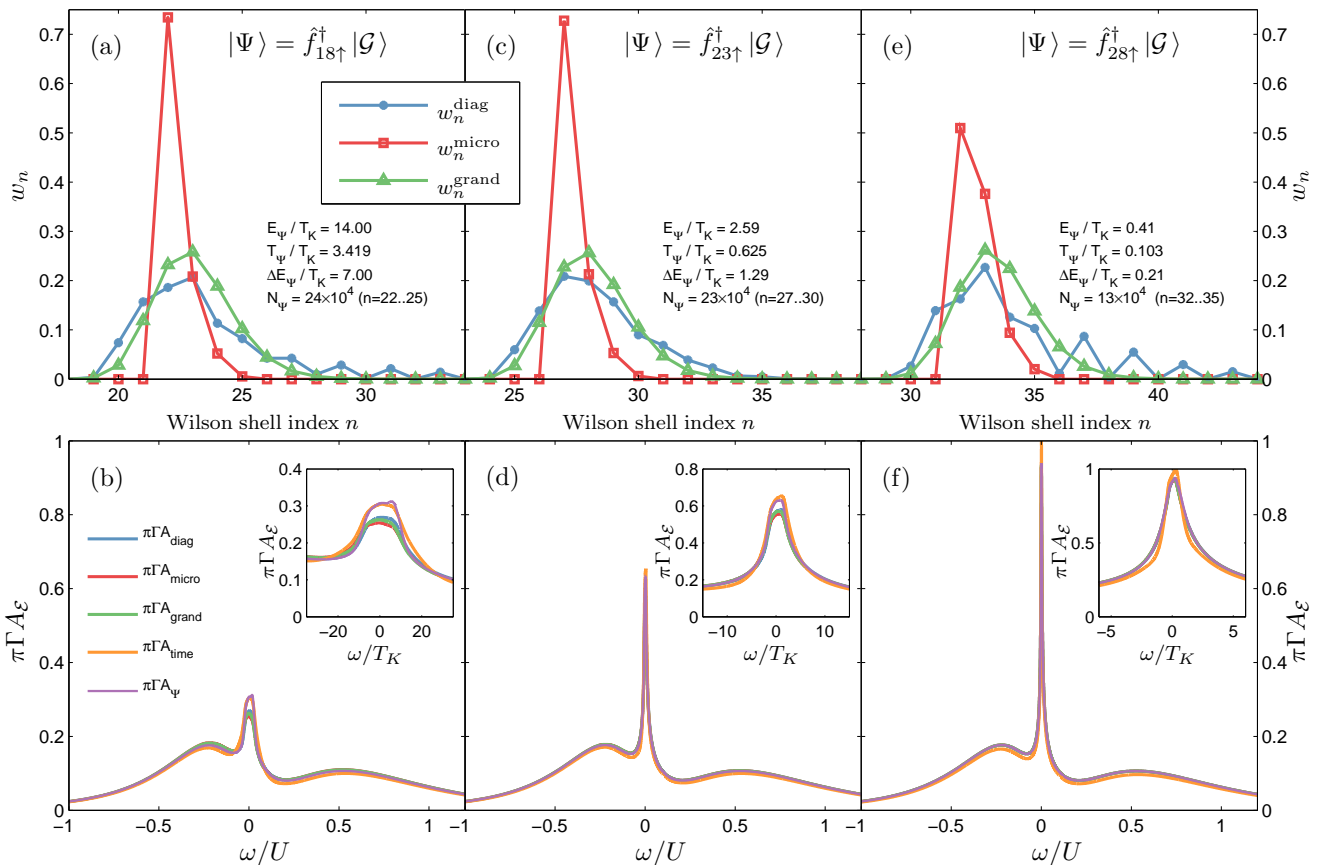


FIG. 3. (color online) The density matrix weight distributions for the diagonal, microcanonical and grand canonical ensembles as a function of the Wilson shell index n (a,c,e), and the normalized spectral functions (b,d,f) calculated for a few excited states obtained after acting with the spin-up creation operator of shell n , $\hat{f}_{n\uparrow}^\dagger$, on the ground state: (a,b) $|\Psi\rangle = \hat{f}_{18\uparrow}^\dagger |\mathcal{G}\rangle$, (c,d) $|\Psi\rangle = \hat{f}_{23\uparrow}^\dagger |\mathcal{G}\rangle$, and (e,f) $|\Psi\rangle = \hat{f}_{28\uparrow}^\dagger |\mathcal{G}\rangle$. The number of states contributing to the microcanonical ensemble is denoted by N_Ψ , where the notation $n = (n_1..n_2)$ indicates the contributing shells. The insets present the zoom of the spectral functions around the Kondo peak.

the Hamiltonian, the diagonal, microcanonical and grand canonical (at temperature $T < \Lambda^{-N/2}$) density matrices have only a single nonzero entry, i.e. from the state, $|se\rangle_n^D = |\mathcal{G}\rangle$. Consequently, by construction, one finds $A_{\text{diag}}^D = A_{\text{micro}} = A_{\text{grand}} = A_\Psi$. In principle, also the time-averaged spectral function A_{time} should be exactly equal to A_Ψ . However, as seen in the inset in Fig. 2, here some small differences arise from the fact that to calculate A_{time} , cf. Eq. (B2), one needs to insert one additional completeness relation (11) as compared to the calculation of A from a density matrix. Due to the NRG approximation in Eq. (11b), indeed, this can lead to slightly different numerical results.

A. Single-particle excitations in the bath

While the eigenstate thermalization hypothesis is trivially satisfied for the ground state of the system (see Fig. 2 above), the validity of ETH is not at all clear for other eigenstates of the system. In the following,

more generally, we analyze thermalization by starting from pure states which are not necessarily also eigenstates of the full Hamiltonian. Here, in particular, we consider excited states of the bath obtained by adding or removing a single particle at energy shell k within the bath on top of the Kondo ground state. To be specific, we consider $|\Psi\rangle = \hat{f}_{k\uparrow}^\dagger |\mathcal{G}\rangle$ with $k = 18, 23, 28$ for the same model parameters as in Fig. 2. The energy of such an excitation is approximately proportional to $\omega_k \simeq D\Lambda^{-k/2}$. For the parameters chosen here, shell $k = n_K \simeq 23$ corresponds to the energy scale of the Kondo temperature T_K , whereas $k = 18$ ($k = 28$) corresponds to a larger (smaller) energy scale, respectively. The spectral functions calculated using different ensembles are displayed in Fig. 3. The top panels present the dependence of weights of the corresponding ensembles on the Wilson shell index n , while the bottom panels show the corresponding spectral functions.

It is instructive to compare the shapes of the spectral functions of these excited states to that of the ground state spectral function in Fig. 2. Since the energies of

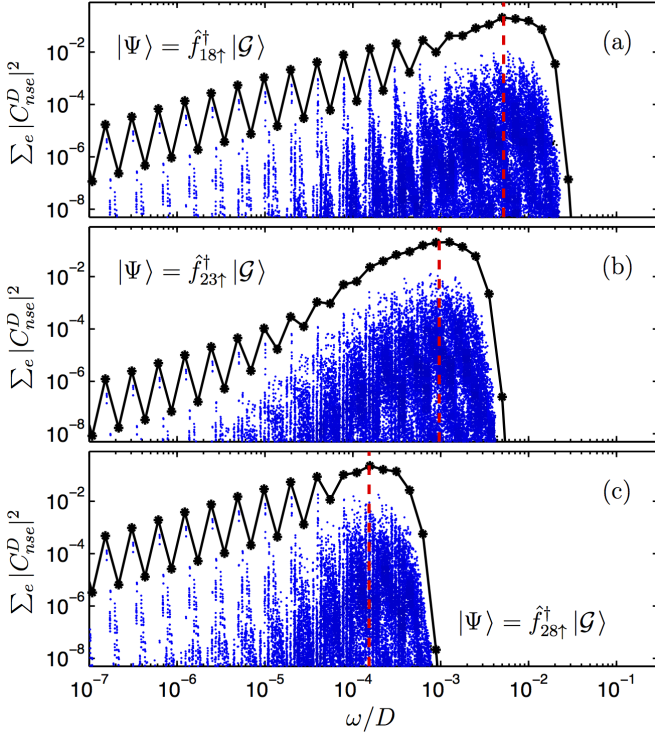


FIG. 4. (color online) The matrix elements of the diagonal density matrix, $\sum_e |C_{nse}^D|^2$, calculated for different excited states, $|\Psi\rangle = \hat{f}_{n\uparrow}^\dagger |\mathcal{G}\rangle$, as indicated in the figure panels. The matrix elements are plotted as a function of energy $\omega \equiv E_{ns}^D$ measured relative to the ground state energy $E_{\mathcal{G}}$. The solid lines display the integrated weights w_n^{diag} of the diagonal ensemble plotted as a function of energy of a given iteration n , $\omega = \alpha \Lambda^{-n/2}$, with α a numerical constant taking into account the energy spread of each iteration. The vertical dashed lines indicate the average energy of state $|\Psi\rangle$, E_Ψ .

these excited states are still significantly smaller than the energies corresponding to the Hubbard resonances, $E_\Psi \ll |\varepsilon_d|, \varepsilon_d + U$, the high-energy features of the spectral functions remain essentially unaltered. What is most affected for given parameter set, is the height of the resonance at the Fermi level, which is a measure of the respective strength of electronic correlations leading to the Kondo effect. As expected, the overall trend seen in the lower panels of Fig. 3 is that for $k < n_K$, the Kondo resonance is significantly suppressed [see Fig. 3(b)], for $k = n_K$, the normalized spectral functions reach approximately one half [see Fig. 3(d)], while for $k > n_K$, the Kondo resonance almost reaches its maximum possible height [see Fig. 3(f)]. In other words, hitting the ground state with an operator acting on energy shell k destroys low-energy correlations at energies $\omega_n \ll \omega_k$, i.e. $n > k$.

Let us now focus more carefully on the particular behavior of A for different ensembles and the implications of our numerical results for the ETH. The first row of Fig. 3 shows the corresponding weights $w_n^\mathcal{E}$ [see Eq. (13)] of the diagonal, microcanonical and grand canonical ensembles. For a given state $|\Psi\rangle = \hat{f}_{k\uparrow}^\dagger |\mathcal{G}\rangle$, throughout,

the normalized weights become nonzero at energy shells $n \gtrsim k$, exhibit a pronounced maximum around $n \sim k + 4$, which is followed by a rapidly decaying tail towards larger n , i.e. smaller energy scales. The shift of the maximum in w_n relative to k depends on Λ , and results from the fact that although the energy of state E_Ψ is comparable to the energy scale of given iteration n , the representative states relevant for the microcanonical ensemble, satisfying $|E_{ns}^D - E_\Psi| \leq \delta E_\Psi$, belong to iterations $n > k$. This also underpins the choice for the effective temperature $T_\Psi \simeq E_\Psi/4$ for the grand canonical ensemble which ensures that $n_{\text{max}}^{\text{grand}} \simeq n_{\text{max}}^{\text{diag}}$.

By construction, the weight distributions w_n^{micro} are significantly narrower, yet also with their maximum at $n_{\text{max}}^{\text{micro}} \sim k + 4$. The number of Wilson shells relevant for the microcanonical ensemble are comparable for all states considered in Fig. 3(a,c,e). In contrast, the weight distributions w_n^{diag} and w_n^{grand} for the diagonal and grand canonical ensemble, respectively, are nonzero over a wider range of shells and spread to the end of chain. Nevertheless, the maximum weight occurs at a comparable energy shell for all these cases, and therefore $n_{\text{max}}^{\text{diag}} \simeq n_{\text{max}}^{\text{micro}} \simeq n_{\text{max}}^{\text{grand}}$. Because of that, all the three ensembles give comparable results, which become basically identical once $k > n_K$ [see Fig. 3(f)]. Therefore with $A_{\text{diag}} \simeq A_{\text{micro}}$, this suggests that for the initial states with single-particle excitations in the bath, A behaves thermally and, in the long time limit, can be described by a proper statistical-mechanical ensemble.

The detailed energy dependence of the matrix elements of the diagonal density matrix $\sum_e |C_{nse}^D|^2$ vs. E_{ns}^D is presented in Fig. 4 for the same three excited states as analyzed in Fig. 3. The overall behavior of the matrix elements $|C_{nse}^D|^2$ is reflected in the integrated weights resulting in the diagonal density ensemble w_n^{diag} (solid lines with bullets). Its distribution is clearly peaked around the average energy E_Ψ (red-dashed vertical lines in Fig. 4), with a *linear* decay towards lower energies. The physical relevance of the latter will be analyzed in detail in Sec. III C and Fig. 13 below.

The long time behavior of the system is approximately described by the microcanonical ensemble. This is demonstrated in Fig. 5 which shows the dependence of the height of the Kondo resonance, $\pi\Gamma A(0)$, on the Wilson shell index k for the initial state $|\Psi\rangle = \hat{f}_{k\uparrow}^\dagger |\mathcal{G}\rangle$. This static observable can be directly related to the linear conductance at given temperature, $G/G_0 = \pi\Gamma A(0)$, with $G_0 = 2e^2/h$. One can see that with increasing k , $\pi\Gamma A(0)$ shows a small resonance for $k \approx 10$, which corresponds to the energy scale of the hybridization Γ . This linear conductance increases further all the way down to the Kondo energy scale $n_K \simeq 23$. For $k > n_K$, finally, $\pi\Gamma A(0)$ saturates and reaches unity. The fact that $A_{\text{diag}} \simeq A_{\text{micro}}$ holds,⁷ supports the eigenstate thermalization hypothesis,^{5,6} which states that the eigenstate expectation values do not fluctuate between eigenstates that are close in energy.

To check whether ETH really holds for our strongly

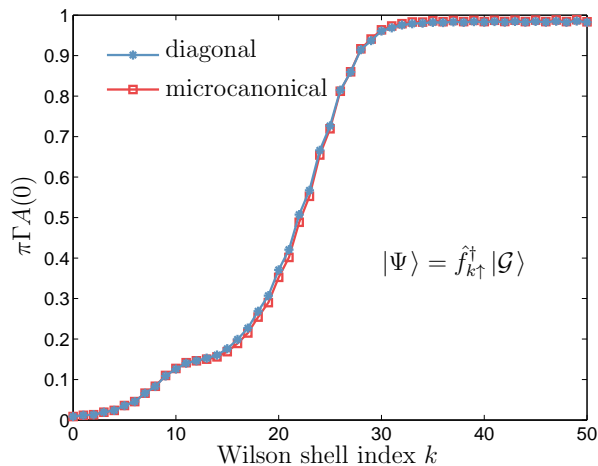


FIG. 5. (color online) The normalized spectral function at energy $\omega = 0$, $\pi\Gamma A(0)$, calculated using the diagonal and microcanonical ensembles for the initial state $|\Psi\rangle = \hat{f}_{k\uparrow}^\dagger|\mathcal{G}\rangle$ as a function of the Wilson shell index k . The spectral data was broadened with $\omega_0 = E_\Psi$. The predictions based on microcanonical ensemble agree reasonably well with those based on the diagonal ensemble, which indicates that the system behaves thermally.

correlated electron system, instead of the above single-particle excited states, we also analyze the behavior of the actual many-body eigenstates. For this purpose, Fig. 6 presents the energy expectation values of two specific physical quantities for individual NRG eigenstates $|E\rangle \equiv |se\rangle_n^D$ relevant for the microcanonical ensemble, i.e. satisfying $|E - E_\Psi| \leq \delta E_\Psi$ for some given reference state $|\Psi\rangle$: Fig. 6(a) shows the plain dot occupation $n_d \equiv \langle E|\hat{n}_d|E\rangle$ with $\hat{n}_d = \sum_\sigma \hat{d}_\sigma^\dagger \hat{d}_\sigma$, where in the thermal case $n_d = \int d\omega A(\omega) f(\omega)$ with $f(\omega)$ the Fermi distribution function, and Fig. 6(b) depicts the normalized spectral function operator \hat{A} taken at energy $\omega = 0$, i.e. $\pi\Gamma \langle E|\hat{A}(0)|E\rangle$.

The expectation values are calculated for the reference state $|\Psi\rangle = \hat{f}_{23\uparrow}^\dagger|\mathcal{G}\rangle$ where the single-particle excitation occurs at the energy shell $k = n_K \simeq 23$ corresponding to T_K . They are compared with the microcanonical expectation values, $\text{Tr}[\hat{\rho}_{\text{micro}}\hat{n}_d]$ and A_{micro} , respectively (see the dashed horizontal lines in Fig. 6). The different colors (symbols) indicate those Wilson shells at which the weights of the microcanonical density matrix are finite [see left inset in Fig. 6(a)]. The largest contribution comes from iteration $n = 27$, where w_n^{micro} is maximum.

Let us first discuss the behavior of the plain expectation value of the dot occupation n_d in Fig. 6(a). While it grows weakly with increasing E , the histogram of the data in the right inset of Fig. 6(a) clearly shows that the energy expectation values are centered at the microcanonical expectation value (vertical dashed lines). The spread of the data is extremely small due to the simplicity of the measured operator which, by itself, is insensitive to Kondo correlations. Overall, however, this clearly in-

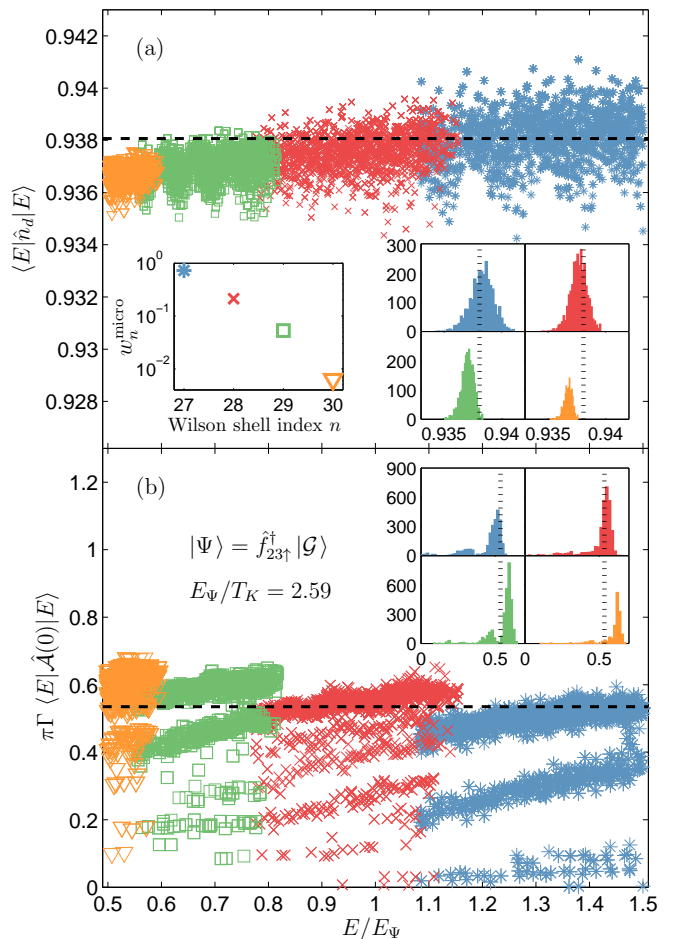


FIG. 6. (color online) Energy-resolved expectation values relevant for the microcanonical ensemble of (a) the dot occupation, $n_d = \langle E|\hat{n}_d|E\rangle$, and (b) the normalized spectral function operator $\pi\Gamma \langle E|\hat{A}(0)|E\rangle$ taken at $\omega = 0$. Here the microcanonical ensemble was based on the initial state $|\Psi\rangle = \hat{f}_{23\uparrow}^\dagger|\mathcal{G}\rangle$, and the energy expectation values are computed for individual energy eigenstates $|E\rangle \equiv |se\rangle_n^D$. For (b), the spectral data was broadened using $\omega_0 = E_\Psi$. The dashed horizontal lines display $\text{Tr}[\hat{\rho}_{\text{micro}}\hat{n}_d]$ and A_{micro} for panel (a) and (b), respectively. The left inset in (a) presents the distribution of weights of the microcanonical density matrix w_n^{micro} on the Wilson chain, where the different symbols differentiate between specific energy shells. The same symbols are also used when plotting the energy expectation values in the main panels. The right insets in (a) and (b) show the corresponding energy-shell resolved histograms of the data from the main panel.

dicates that for given operator the knowledge of a single energy-eigenstate within a narrow energy window is sufficient to find the expectation value $\langle \hat{n}_d \rangle$ in the long-time limit.

In contrast, the energy expectation value of the normalized spectral operator at the Fermi level, $\pi\Gamma \hat{A}(0)$, is significantly more sensitive to the specific energy eigenstate, as shown in Fig. 6(b). The reason for this is that in given case, by construction, $\pi\Gamma \hat{A}(0)$ derives from a

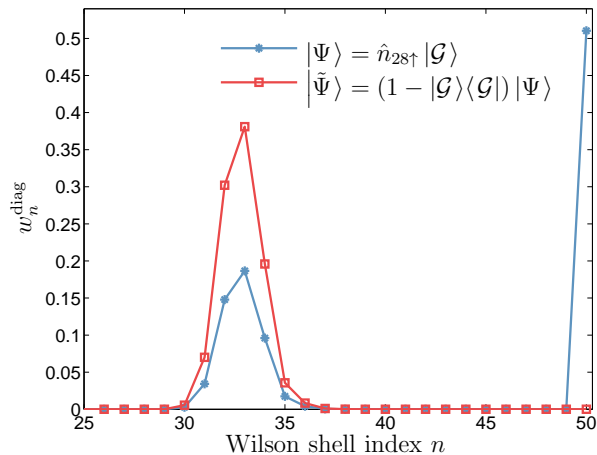


FIG. 7. (color online) The weights of the diagonal ensemble w_n^{diag} as a function of the Wilson shell index n calculated for states $|\Psi\rangle = \hat{n}_{28\uparrow}|\mathcal{G}\rangle$ and $|\tilde{\Psi}\rangle = (1 - |\mathcal{G}\rangle\langle\mathcal{G}|)|\Psi\rangle$.

dynamical correlator that is strongly sensitive to Kondo correlations. In Fig. 6(b), due to the discrete nature of the Wilson chain at intermediate iteration n , the data appears in bunches. Similar to Fig. 6(a), each of these bunches shows a slight upward trend with increasing energy E , while the overall trend from shell to shell is slightly downward. Nevertheless, although the fluctuations of the data are larger than in Fig. 6(a), the main contribution is centered at the microcanonical expectation value, A_{micro} , as seen in the insets to Fig. 6(b). This again suggests that the ETH can be invoked as the mechanism responsible for thermalization in the considered system. The knowledge of an expectation value for a representative energy eigenstate, i.e. an energy eigenstate $|E\rangle$ around E_{Ψ} satisfying $|E - E_{\Psi}| \leq \delta E_{\Psi}$, can be thus used to predict the behavior of the system in the long-time limit.

B. Density excitations in the bath

We now study the process of thermalization and time evolution for initial states obtained after acting with a single-particle *density* operator onto the ground state of the system, $|\Psi\rangle = \hat{n}_{k\uparrow}|\mathcal{G}\rangle$ with $\hat{n}_{k\uparrow} \equiv \hat{f}_{k\uparrow}^\dagger \hat{f}_{k\uparrow}$. This corresponds to a projection of the ground state $|\mathcal{G}\rangle$ onto its component where site $(k\uparrow)$ is fully occupied. The weights of the diagonal density matrix w_n^{diag} for $k = 28$ are shown in Fig. 7. The distribution of w_n^{diag} has a maximum for iterations slightly larger than the Wilson shell on which the density operator acts, yet also has a delta-like contribution at the very end of the finite Wilson chain of length N considered. In fact, approximately half of the weight is transferred to the last shell $n = N$. This can be understood by realizing that for given case $w_n^{\text{diag}} = \sum_{se} |{}_n^D \langle se | \hat{n}_{k\uparrow} | \mathcal{G} \rangle|^2$ has a singular static contribution for $|se\rangle_n = |\mathcal{G}\rangle$, namely $|\langle \mathcal{G} | \hat{n}_{k\uparrow} | \mathcal{G} \rangle|^2 \simeq 1/4$ due to half-filling which, after including the normalization of

$|\Psi\rangle$ above, becomes $\sim 1/2$. This simple static contribution needs to be dealt with separately. The remainder gives rise to a broad distribution around the excitation energy.

For the discussion of statistical ensembles, we focus on the latter term only. For this, we project out the ground state and use the state $|\tilde{\Psi}\rangle = (1 - |\mathcal{G}\rangle\langle\mathcal{G}|)|\Psi\rangle$ to study the process of thermalization [in practice, this state $|\tilde{\Psi}\rangle$ can be constructed exactly by orthonormalizing both states, $|\Psi\rangle$ as well as $\langle\mathcal{G}|\Psi\rangle|\mathcal{G}\rangle$ towards the Wilson shell k at which the excitation was created, and then perform the orthonormalization of $|\Psi\rangle$ with respect to representation of $|\mathcal{G}\rangle$ there]. The resulting weight distribution for state $|\tilde{\Psi}\rangle$ is shown in Fig. 7. This now again resembles the distribution of a thermal ensemble. We have studied the expectation values of the spectral operator for state $|\tilde{\Psi}\rangle = (1 - |\mathcal{G}\rangle\langle\mathcal{G}|)\hat{n}_{k\uparrow}|\mathcal{G}\rangle$ as a function of the Wilson shell index k (not shown), and found that again for all k the microcanonical ensemble describes very well the behavior of the system in the long-time limit.

C. Relevance of microscopic quantum quenches and Anderson orthogonality

The ensembles in Sec. III A (Fig. 3) were constructed from a single particle excitation onto the ground state of the system. Foremost, this corresponds to a microscopic quantum quench at zero temperature. The spectral functions A_{time} and A_{Ψ} analyzed in Fig. 3, are based on the states $|\Psi\rangle$ with or without time-evolution with respect to the full Hamiltonian, respectively. Nevertheless, after real-time evolution to infinite times (see also diagonal ensemble) the Kondo resonance at $\omega = 0$ is not fully restored with only a slight difference between A_{Ψ} and A_{time} [Figs. 3(b) and 3(d)]. This is essentially due to the fact that the Hilbert space, although exponentially large, is based on a coarse-grained bath through the logarithmic discretization parameter Λ of NRG. Consequently, the energy of a microscopic excitation cannot be fully dissipated to infinity, and one can only resolve the physics at energy approximately equal or larger than the corresponding excitation energy. This is in agreement with the simple fact³¹ that Wilson chains are not true thermal reservoirs and as such cannot fully transfer local microscopic energy to infinity. In particular, due to the lack of real-space association within the Wilson chain, energy cannot be dissipated to the end of the chain since for a given Wilson shell n , all shells $n' > n$ represent and thus can absorb only exponentially small energy $\propto \Lambda^{-n/2}$. Therefore due to the exponential decrease of hopping matrix elements along the Wilson chain, the energy of an excitation that is created at a given site cannot travel away very far in either direction along the Wilson chain, since there is an energy mismatch in both directions [(see also Fig. 12 below).

A microscopic local quantum quench within a Fermi sea can also be analyzed through the viewpoint of An-

derson orthogonality (AO).^{32–34} The decay of the overlap of ground state wave functions for initial (I) and final (F) state, $|\Psi_I\rangle$ and $|\Psi_F\rangle$, respectively, is given by³²

$$|\langle\Psi_I|\Psi_F\rangle|^2 \propto \left(\frac{1}{L}\right)^{-\Delta n_{\text{loc}}^2} \quad (17a)$$

where³³

$$\frac{1}{L} \propto \omega(n) \propto \Lambda^{-\frac{n}{2}}, \quad (17b)$$

with L the system size, and $\frac{1}{L} \propto \omega(n)$ the finite size level-spacing. Hence in the NRG context, for a Wilson chain of linear length n translates into an *exponentially* large (effective) system sizes. Therefore the AO power law decay in Eq. (17a) translates into an exponential decay along the Wilson chain.³³ When plotted vs. the energy scale ω_n , the fitted exponent reflects the charge Δn_{loc} that is displaced to or from infinity. For example, the exponent seen in Fig. 4 for small energies ω suggests $|\Delta n_{\text{loc}}| = 1$, which is in perfect agreement with the fact that the extra particle $\hat{f}_{n\sigma}^\dagger$ that has been inserted in $|\Psi_I\rangle = \hat{f}_{n\uparrow}^\dagger|\mathcal{G}\rangle$ will be dissipated to infinity.

The decay of the wave function overlap in Eq. (17a), is not necessarily constrained to the overlap of explicit ground state wave functions. In particular, it describes an arbitrary local quantum quench,³⁴ say at time $t = 0$, on top of the ground state of given (final) Hamiltonian $[|\Psi(t=0)\rangle = |\Psi_I\rangle]$ can be considered the ground state of a fictitious initial Hamiltonian. As time proceeds, a larger and larger volume L will be affected through the quantum quench, which justifies the association that $L \sim v_F t \propto 1/\omega$, with v_F the Fermi velocity.

Furthermore, the overlap in Eq. (17a) can be computed with respect to an ensemble average at given energy scale $\omega_n \propto 1/L$,³³ and thus the l.h.s. of Eq. (17a) directly relates to the diagonal weight distributions w_n^{diag} .

$$w_{n:F}^{\text{diag}} \propto \rho_{n:I}^{\text{diag}} \cdot \left(\frac{1}{L}\right)^{-\Delta n_{\text{loc}}^2}, \quad (18)$$

where $\rho_{n:I}^{\text{diag}} \equiv \sum_{n' \geq n} w_{n':I}^{\text{diag}}$ describes the cumulative weight of the diagonal density matrix of the initial system for shells $n' \geq n$. Therefore adding or removing a particle strongly affects the weight distributions w_n^{diag} of the final state. This is the underlying mechanism that essentially allows the very different earlier interpretation above of a (close to) thermalized state, despite having applied a microscopic single particle excitation. There the resulting state mimics a macroscopic ensemble while caveats apply (see Sec. III D below). All of this, of course, is very specific and hence tightly connected to the underlying logarithmic discretization and hence to the NRG perspective.

While in the above sense, Fig. 3 does allow an approximate effective interpretation of single-particle excitations within the Wilson bath in terms of effective thermodynamic ensembles (a more careful analysis will be given in Sec. III D below), clearly, this interpretation is not always possible. Motivated by above AO based arguments,

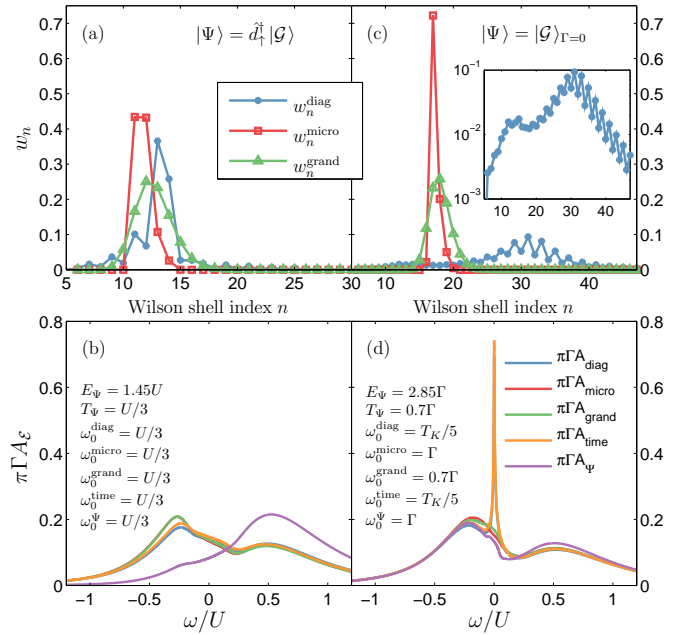


FIG. 8. (color online) Weight distribution of various ensembles (upper panels) and the corresponding normalized spectral function $\pi\Gamma A_\mathcal{E}$ (lower panels) for the state $|\Psi\rangle = \hat{d}_\uparrow^\dagger|\mathcal{G}\rangle$ (left panels) and $|\Psi\rangle = |\mathcal{G}\rangle_{\Gamma=0}$ (right panels). The grand canonical spectral function was calculated at an effective temperature T_Ψ specified in the figure, together with $\omega_0^{\text{grand}} = T_\Psi$. For the other spectral functions, A_{diag} , A_{micro} , A_{time} , and A_Ψ , we optimized the broadening parameters such that all unphysical features due to discretization were smeared out, with the respective values for ω_0^{diag} , ω_0^{micro} , ω_0^{time} , and ω_0^Ψ specified in the panels. The inset to panel (c) shows the weights of the diagonal ensemble w_n^{diag} plotted on logarithmic scale as a function of Wilson shell index.

in the following we contrast two local quantum quenches at the impurity: (i) using $|\Psi\rangle = \hat{d}_\uparrow^\dagger|\mathcal{G}\rangle$, and (ii) using the ground state of the decoupled bath, $|\Psi\rangle = |\mathcal{G}\rangle_{\Gamma=0}$, which is equivalent to a quantum quench by turning on Γ . The former inserts a particle, while the latter turns on the hybridization of the impurity which mostly results in only local rearrangement of charge.

Figure 8 presents the weight distributions of the corresponding ensembles and the spectral functions. The analysis of the state $|\Psi_b\rangle = \hat{d}_\uparrow^\dagger|\mathcal{G}\rangle$ [Fig. 8(a,b)] is similar in spirit to the analysis in Fig. 3, with the minor difference that the single-particle excitation does not occur within the logarithmically discretized bath through the application of some operator $\hat{f}_{k\uparrow}^\dagger$ which is delocalized in real space, but rather through the application of \hat{d}_\uparrow^\dagger which acts locally at the impurity itself. Therefore the initial spectral function A_Ψ shows significant shift of spectral weight from the lower towards the upper Hubbard resonance at $\omega/U \simeq 0.6$ since by creating an extra particle in the dot enhances the double occupancy. Over time, however, this again relaxes back to the lower Hubbard resonance [see Fig. 8(b)]. Furthermore, by having adding

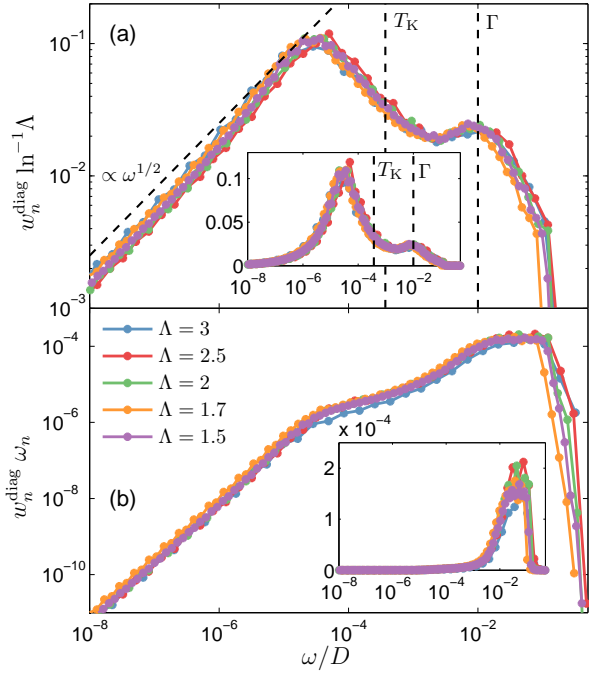


FIG. 9. (color online) (a) The weights of the diagonal density matrix w_n^{diag} and (b) the total energy $E_\Psi \simeq w_n^{\text{diag}} \omega_n$ calculated for the state $|\Psi\rangle = |\mathcal{G}\rangle_{\Gamma=0}$ and plotted as a function of energy $\omega \propto \alpha_\Lambda \Lambda^{-n/2}$, with α_Λ constant of the order of unity chosen in such a way that the maximum of weight distribution occurs at the same energy for all values of Λ presented in the figure. The insets show the corresponding data plotted on the y -axis linear scale. The vertical dashed lines in (a) and its inset mark the energy scales corresponding to T_K and Γ , respectively.

a particle, its charge eventually has to be dissipated to infinity. Hence similar to Fig. 3, starting from the energy scale of the excitation, i.e. quantum quench, strong AO effects again cut off the weight distribution towards later Wilson shells. Therefore all the weight distributions and the spectral functions for the different statistical ensembles show similar behavior, including $A_{\text{diag}} \simeq A_{\text{micro}}$.

Now consider the dynamics starting from the decoupled quantum dot in the state $|\Psi\rangle = |\mathcal{G}\rangle_{\Gamma=0}$ [Figs. 8(c,d)]. Since there are no Kondo correlations in the initial state $|\Psi\rangle$, clearly, A_Ψ shows no Kondo resonance at all. Using an effective temperature such that $E_\Psi = \text{Tr}(\hat{\rho}_{\text{grand}} \hat{H}) \simeq 2.85\Gamma$, this leads to $T_\Psi \simeq 0.7\Gamma \gg T_K$. Therefore the Kondo resonance is clearly also absent in the grand canonical spectral function. For the same reason, the results for the microcanonical spectral function are also very similar. As seen in Fig. 8(c), both have a maximum in their weight distribution at early iterations which correspond to the energy scale of Γ .

In stark contrast, however, the weight distribution for the diagonal ensemble in Fig. 8(c) has its maximum significantly shifted to later energy shells, which clearly lies beyond $n_K \simeq 23$. As a direct consequence, the spectral data in panel (d) clearly shows an emerging Kondo

resonance. Overall, this results in a strong mismatch $A_{\text{diag}} \neq A_{\text{micro}}$, which contradicts and thus cannot be explained through ETH. Instead, here only the elementary description in terms of a microscopic quantum quench in Γ applies: by dissipating the inserted microscopic energy to infinity, from the point of view of the impurity the system returns to its fully interacting ground state. In this view, however one would expect that the Kondo resonance fully reemerges in the thermodynamic limit. Nevertheless, in Fig. 8(d), a somewhat suppressed Kondo peak is seen for A_{diag} as compared to $T = 0$ (see Fig. 2). Because w_n^{diag} is peaked around T_K , the spectral data for smaller energies is limited due to the lack of spectral resolution for $\omega \ll T_K$ for NRG specific technical reasons. A more careful inspection of the weight distribution w_n^{diag} [see inset to Fig. 8(c)] also reveals an enhanced weight around the energy scale of Γ ($n \approx 13$). This is required since for the non-interacting bath under consideration, even in the continuous i.e. non-discretized model, particle or particle-hole excitations which are generated close to the impurity at finite energy, can be emitted to spatial infinity. There, however, they represent long-lived particles due to the absence of interaction, and hence no longer thermalize. This is precisely also reflected within the NRG, where the Wilson chain represents a closed yet exponentially large system. Being discrete, the energy $E_\Psi \sim \Gamma$ must be contained around its respective energy shell.

The energy dependence of the diagonal weight distribution for different discretization parameter Λ is explicitly shown in Fig. 9(a). The weights are plotted as a function of $\omega = \alpha_\Lambda \Lambda^{-n/2}$, with $\alpha_\Lambda \sim 1$ being a constant of the order of unity chosen such that the maximum in w_n^{diag} occurs at the same energy for all values of Λ considered in the figure. Clearly, irrespective of Λ , the structure of the weight distribution *remains exactly the same* and features two peaks: the first one occurs for energies of the order of the coupling strength $\omega \approx \Gamma$, while the second one is located around $\omega \approx T_K$. Since the total energy is given by $E_\Psi \simeq w_n^{\text{diag}} \omega_n$, with $\omega_n \propto \Lambda^{-n/2}$, almost all energy (more than 99%) is carried by the weight for iterations up to $n' \lesssim n_K$ ($\omega \lesssim T_K$), see Fig. 9(b). The peak around $\omega \approx T_K$ and with it the drop of the weight distribution for $n > n_K$ ($\omega < T_K$), finally, again can be understood through Anderson orthogonality: The initial state ($\Gamma = 0$) has no Kondo correlations at all, while the final state develops a fully screened impurity spin, i.e. a Kondo singlet. This is associated with a phase shift of $\pi/2$, or equivalently, an effective shift in local charge by half a charge for spin-up and spin-down, individually. This is clearly also reflected in the AO exponent derived for small energies ω , as shown in Fig. 9(a). In summary, in given case of $|\Psi\rangle = |\mathcal{G}\rangle_{\Gamma=0}$, the effective temperature is therefore *not* set by E_Ψ . Rather, from the point of view of the impurity, the system can be interpreted as having an effective approximate temperature of $T_\Psi^* \lesssim T_K$ superimposed with the single-particle excitations that moved to spatial infinity. Therefore $E_\Psi \gg T_\Psi^*$. This is the rea-

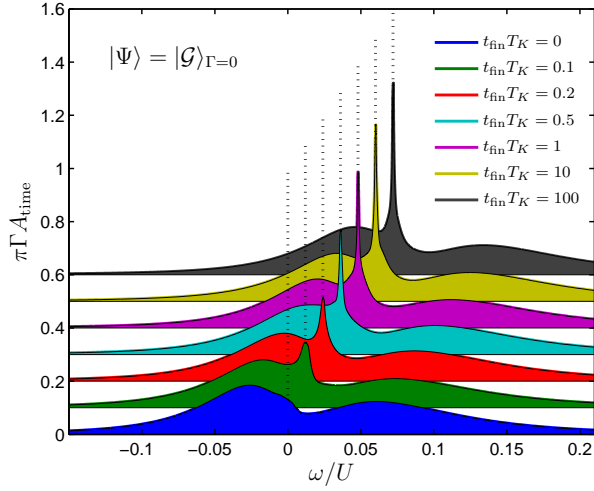


FIG. 10. (color online) The normalized spectral function for the time-evolved state A_{time} starting from $|\Psi\rangle = |\mathcal{G}\rangle_{\Gamma=0}$ calculated at different final times t_{fin} as indicated in the figure. The spectral data was broadened with time-dependent broadening parameter, $\omega_0 = \max(1/t_{\text{fin}}, T_K)$, with $\omega_0 = \Gamma$ for $t_{\text{fin}} = 0$, and averaged over time interval $(t_{\text{fin}} - \delta t, t_{\text{fin}})$, with $\delta t = 0.2t_{\text{fin}}$. The spectral functions are shifted by 0.01 (0.1) in the x-axis (y-axis) to increase visibility.

son why in this case $A_{\text{diag}} \neq A_{\text{micro}}$.

The emergence of the Kondo resonance in the spectral function as a function of time for $|\Psi\rangle = |\mathcal{G}\rangle_{\Gamma=0}$ at $t = 0$ is explicitly shown in Fig. 10. There A_{time} is calculated at different final times t_{fin} using $\omega_0 = \max(1/t_{\text{fin}}, T_K)$. As expected, the characteristic time scale, at which the Kondo correlations develop, is of the order of $t_{\text{fin}} \sim 1/T_K$. In the long-time limit, the Kondo resonance saturates at the height $\pi\Gamma A_{\text{time}}(0) \sim 0.7$ which, indeed, is consistent with an effective temperature $T_{\Psi}^* \lesssim T_K$. This long-time limit of A_{time} , by construction, is equivalent to the spectral function A_{diag} [see Fig. 8(d)].

Summarizing Sec. III A to Sec. III C, microscopic quantum quenches first and foremost need to be viewed from the perspective of Anderson orthogonality. Their interpretation in terms of a thermalization to a macroscopic statistical ensemble is peculiar to the logarithmic discretization underlying NRG as will be analyzed in more detail next.

D. Thermodynamic limit

Thermalization of a macroscopic system in the ground state to finite temperature through application of a single-particle (written as 1-particle below) excitation appears like a contradiction. Nevertheless, for standard discretization parameters (i.e. $\Lambda \gtrsim 2$), NRG comes very close to this description. On the other hand, in the thermodynamic limit $\Lambda \rightarrow 1^+$, this prescription must fail and, eventually, macroscopically many 1-particle excitations will be required for thermalization. While the location

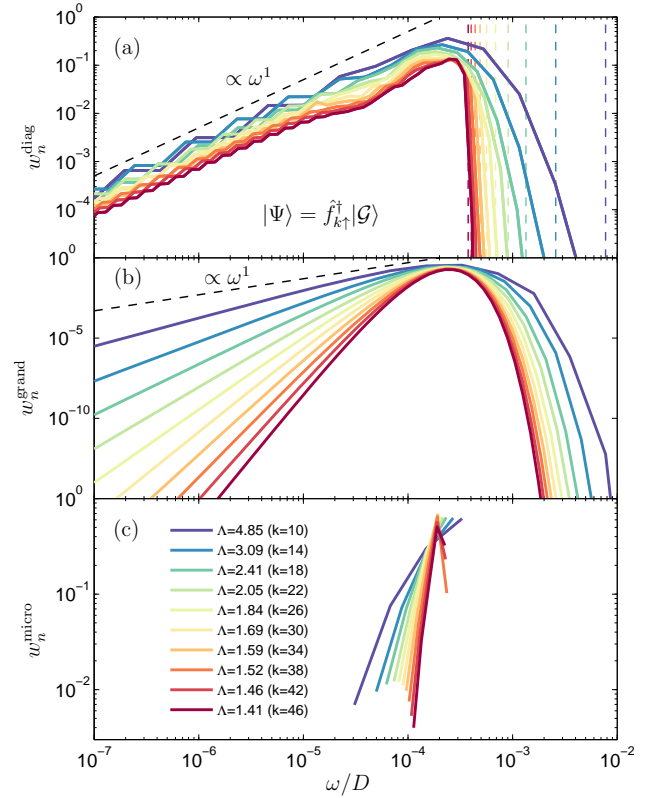


FIG. 11. (color online) The weight distributions of (a) the diagonal w_n^{diag} , (b) the grand canonical w_n^{grand} and (c) the microcanonical w_n^{micro} density matrices as a function of energy $\omega = \alpha_{\Lambda} \Lambda^{-n/2}$, with α_{Λ} of order 1 (see text). These distributions were calculated after application of a single 1-particle excitation $|\Psi\rangle = \hat{f}_{k\uparrow}^{\dagger} |\mathcal{G}\rangle$ at shell k , where for a given Wilson energy shell k , the discretization parameter Λ was chosen such that the excitation occurred at comparable energy, i.e. $\Lambda(k) = E^{-2/k}$ for $E = T_K$. The vertical dashed lines in (a) present the corresponding energies at which the excitation occurred.

of the maxima in the weight distribution w_n along the Wilson energy shells essentially will remain unaltered, the clear difference will be in the tails of these weight distributions. Therefore this section is devoted to the discussion of the behavior of these tails for different discrete coarse-graining Λ , as well as their behavior after subsequent multiple 1-particle excitations towards exact thermalization. For the sake of energy scale separation, however, in practice $\Lambda \gtrsim 1.4$ will be used.

1. Single 1-particle excitation

Figure 11 shows the weights of the diagonal, grand canonical and microcanonical density matrices calculated for a single 1-particle excitation, $|\Psi\rangle = \hat{f}_{k\uparrow}^{\dagger} |\mathcal{G}\rangle$, for different values of the discretization parameter Λ . The discretization parameter was chosen such that the excitations occurred at comparable energy, i.e. $\Lambda(k) = E^{-2/k}$

for fixed $E = T_K$. The weights are plotted as a function of energy $\omega = \alpha_\Lambda \Lambda^{-n/2}$, where α_Λ is a discretization dependent but otherwise constant factor of order 1, chosen such that the maximum of w_n^{grand} occurs at the same energy for all Λ . The vertical dashed lines in Fig. 11(a) show the corresponding energies E_Ψ , at which the excitation was created, which without rescaling by α_Λ would have occurred at approximately the same energy. The weights of the diagonal ensemble in Fig. 11(a) were averaged over two consecutive Wilson shells to suppress the otherwise strong even-odd oscillations, in particular, for larger Λ . In stark contrast, w_n^{grand} in Fig. 11(b) does not exhibit even-odd effects.³⁵

By construction, the behavior of the weight for the microcanonical ensemble in Fig. 11(c) is entirely different from w_n^{diag} and w_n^{grand} , in that w_n^{micro} is nonzero only in a narrow energy window. Hence the following discussion will focus on w_n^{diag} and w_n^{grand} in panels (a) and (b), respectively. Also, as seen in Fig. 11(a), the decay of the weight distribution at large energies, i.e. for energies larger than those at which the weight maximum occurs, is extremely fast for both w_n^{diag} and w_n^{grand} , much faster than power-law or even exponential. In fact, by construction, w_n^{diag} becomes strictly zero for Wilson shells larger than the shell at which the excitation occurred.

In contrast, the decay for small energies, shows characteristic powerlaw behavior. As seen in Fig. 11(a), w_n^{diag} decays linearly for small ω , i.e. $w_n^{\text{diag}} \propto \omega^1$, which is thus independent of Λ . This is contrary to w_n^{grand} [Fig. 11(b)], which decays with n like d^{-n} ,^{27,35} for small energies (i.e. large n), where $d = 4$ is the dimension of the local state space of a single Wilson site. Hence when plotted vs. ω , w_n^{grand} becomes dependent on the discretization parameter Λ . With the slope for small ω in Fig. 11(b) decreasing with increasing Λ , the slopes of w_n^{diag} and w_n^{grand} eventually coincide for large $\Lambda = d^2$ (having $d = 4$ here, $\Lambda = 16$; not shown). Then, the diagonal and grand canonical density matrices will have similar dependence on energy, and therefore a single 1-particle excitation suffices to immediately thermalize the system. However, with decreasing Λ , more and more single-particle excitations will be required to fully thermalize the system. Nevertheless, as will be shown below, for a typical value of $\Lambda \geq 2$, still a very few 1-particle excitations suffice to thermalize the system.

2. Multiple 1-particle excitations

In Fig. 12 we show the occupations of the Wilson chain as a function of shell index n , computed through $\langle \Psi | \hat{n}_{n\sigma} | \Psi \rangle$ and also by using the diagonal density matrix, $\text{Tr}[\hat{\rho}_{\text{diag}} \hat{n}_{n\sigma}]$, which describes the effective long-time limit after a quench by a local excitation. These occupations are calculated for three values of discretization parameter $\Lambda \in \{1.5, 2, 3\}$ in panels (a), (b), and (c), respectively.

We start by analyzing a state with a single excitation,

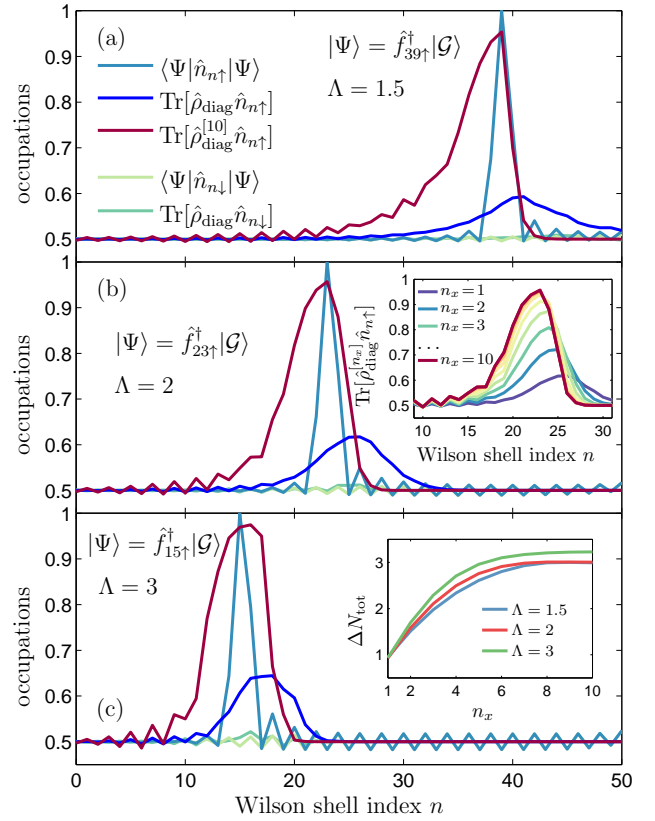


FIG. 12. (color online) The occupations on the Wilson chain for (a) $\Lambda = 1.5$, (b) $\Lambda = 2$ and (c) $\Lambda = 3$ calculated for initial state (a) $|\Psi\rangle = \hat{f}_{39}^\dagger |\mathcal{G}\rangle$, (b) $|\Psi\rangle = \hat{f}_{23}^\dagger |\mathcal{G}\rangle$ and (c) $|\Psi\rangle = \hat{f}_{15}^\dagger |\mathcal{G}\rangle$ and for diagonal ensemble as a function of the Wilson shell index n . The excitation was created at the same energy scale for all Λ . The spin-up occupations obtained using $\hat{\rho}_{\text{diag}}$ after having applied $n_x = 10$ single-particle excitations are shown for comparison. The inset in (b) presents the buildup of spin-up charge vs. shell index n when applying up to a total of n_x excitations. The inset in (c) shows the change of the total charge of the system ΔN_{tot} as a function of n_x .

i.e. $n_x = 1$ with $|\Psi\rangle = \hat{f}_{k\uparrow}^\dagger |\mathcal{G}\rangle$, where the Wilson shell k at which the operator acts, was chosen such that the excitation energy was comparable ($\sim T_K$) for all Λ . Thus, for $\Lambda = 1.5$ [Fig. 12(a)] the excitation was created at shell $k = 39$, for $\Lambda = 2$ [Fig. 12(b)] at $k = 23$, and for $\Lambda = 3$ [Fig. 12(c)] at $k = 15$. Irrespective of the value of discretization parameter, the behavior of the chain occupations is qualitatively the same. First, since the spin-up creation operator was applied, the spin-down occupations are hardly affected. Second, $\langle \Psi | \hat{n}_{n\uparrow} | \Psi \rangle$ reaches unity at the shell k on which the excitation was created and then for $n > k$, it shows somewhat more pronounced even-odd oscillations. Third, after having evolved the system to infinite time, the additional particle that had been inserted locally, smears over several Wilson shells. However, the underlying logarithmic discretization of the Wilson chain prohibits the particle to leave the range of sites that represent its energy shell.

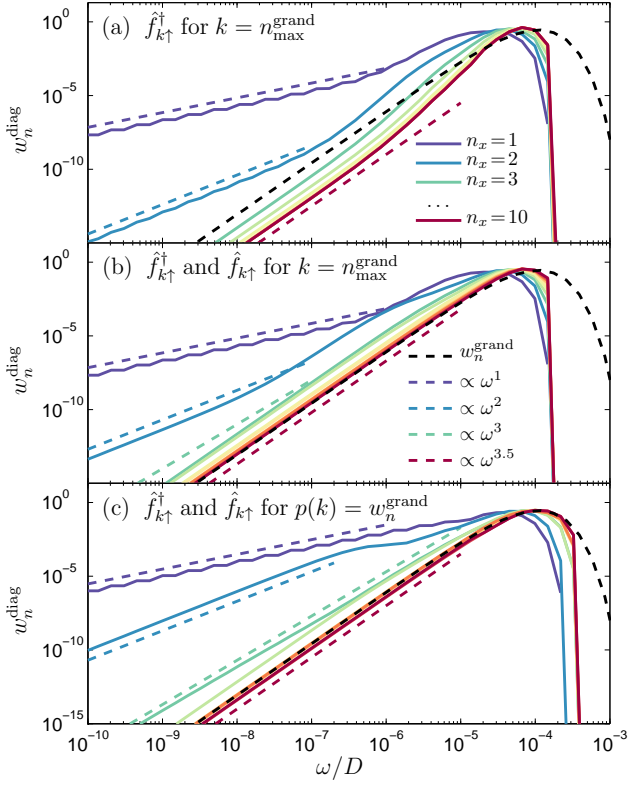


FIG. 13. (color online) The weights of the diagonal w_n^{diag} density matrix plotted on logarithmic scale as a function of energy $\omega \propto \Lambda^{-n/2}$ calculated for single-particle excitations applied to the ground state ($n_x = 1$) and then consecutively to the diagonal density matrix ($n_x > 1$). In (a) $\hat{f}_{k\uparrow}^\dagger$ was applied at shell $n_{\text{max}}^{\text{grand}}$, at which w_n^{grand} is maximum. In (b) the operators $\hat{f}_{k\uparrow}^\dagger$ and $\hat{f}_{k\uparrow}$ were applied at shell $n_{\text{max}}^{\text{grand}}$ in an alternating way, whereas in (c) the same operators were applied with probability $p(k)$ determined by w_n^{grand} . The dashed lines show the corresponding asymptotic lines. After $n_x \gtrsim 5$ excitations the slope of w_n^{diag} becomes equal to that of w_n^{grand} (black dashed line). This figure was calculated for $\Lambda = 2.21$, for which the dependence of w_n^{grand} on energy is $w_n^{\text{grand}} \propto \omega^{3.5}$.

As discussed above, within the NRG, a single 1-particle excitation is typically close but not exactly sufficient to fully thermalize the system for typical values of the discretization parameter $\Lambda \gtrsim 2$. We therefore test if it is possible to thermalize the system by sequential application of multiple 1-particle excitations with intermediate relaxation. For this, we start with the system in its ground state, to which a first 1-particle excitation is applied ($n_x = 1$) at some shell k that resembles the energy scale of a fixed temperature $T = T_K$. After we allow the system to equilibrate, i. e. to time-evolve to $t \rightarrow \infty$, it is described by the corresponding diagonal ensemble, i. e. the diagonal density matrix $\hat{\rho}_{\text{diag}}^{[1]} \equiv \hat{\rho}_{\text{diag}}$ and the weights $w_n^{\text{diag}} \equiv w_{[1];n}^{\text{diag}}$. Now given this state, which is no longer described by a pure density matrix, we apply a second 1-particle operator ($n_x = 2$), and again let it time-evolve to infinity. This generates a new diagonal en-

semble described by the density matrix $\hat{\rho}_{\text{diag}}^{[2]}$ and weights $w_{[2];n}^{\text{diag}}$. This procedure can be repeated up to a total of n_x excitations applied to the system, which results in the equilibrated diagonal ensemble $\hat{\rho}_{\text{diag}}^{[n_x]}$, represented by the weight distribution $w_{[n_x];n}^{\text{diag}}$. The underlying MPS diagrams that describe the required numerical procedures are discussed in detail in App. C.

The occupations of the Wilson chain as a function of shell index n for different number n_x of 1-particle excitations applied to the system are shown in the inset of Fig. 12(b), while $\text{Tr}[\hat{\rho}_{\text{diag}}^{[10]} \hat{n}_{n\uparrow}]$ is additionally shown in each panel of Fig. 12. One can see that repeated application of the same spin-up creation operator at the same shell k leads to an increase of the overall occupation for spin-up. This increase, however, quickly saturates, as seen in the analysis of the change of the total number of particles on the Wilson chain ΔN_{tot} in the inset to Fig. 12(c). For the rather broad range of discretizations analyzed, $\Lambda \in [1.5, 3]$, repeated application of the same creation operator with intermediate equilibration allows to insert a total of at most three particles into the system due to the underlying logarithmic discretization. For the well-saturated value of $n_x = 10$, the inserted particles remain in the close vicinity of the shell that it has been inserted.

A more detailed behavior of the system is provided by the weights of the diagonal ensemble, which are shown in Fig. 13 as a function of energy $\omega \propto \Lambda^{-n/2}$, for different number n_x of excitations created in the system. The case when the same spin-up creation operator was applied to the shell at which the grand canonical weights has its maximum, $k = n_{\text{max}}^{\text{grand}}$, is presented in Fig. 13(a). One can see that for $n_x = 1$ the low-energy tail of w_n^{diag} scales linearly with energy [this exactly reflects the situation already seen in Fig. 11(a)]. Now after applying the same operator a second time ($n_x = 2$), the low-energy dependence changes to $\propto \omega^2$, and finally after $n_x \gtrsim 4$, the slope of w_n^{diag} saturates and coincides with that of w_n^{grand} (at ultrasmall ω , $n_x = 3$ still bends over to a ω^3 powerlaw behavior; not shown). Similar behavior can be observed when both creation and annihilation operators are applied in an alternating way to the same shell $k = n_{\text{max}}^{\text{grand}}$, yet as always with intermediate relaxation [see Fig. 13(b)]. Figure 13(c), finally, also relaxes the constraint of fixed k , in that creation and annihilation operators are applied alternatively at shell k where k is chosen with probability $p(k)$ determined by the distribution of w_n^{grand} calculated at temperature $T_{\text{grand}} = T_K$. With this, the behavior of w_n^{diag} becomes even more similar to that of w_n^{grand} . The remaining sharp truncation of the distribution towards large ω is due the finite sampling in n_x . But as seen in Fig. 13(c), this edge can be moved towards larger frequencies (Wilson shells).

Note that the increasing exponent in the power law $\propto \omega^{n_x}$ for the low energy behavior of the diagonal weight distribution after n_x applications of local creation or annihilation operators with intermediate relaxation is per-

fectly consistent with the concept of AO as indicated in Eq. (18): with $\rho_{n;I=n_x}^{\text{diag}} \propto \omega^{-n_x}$ and $\Delta n_{\text{loc}} = 1$, it follows $w_{n;n_x+1}^{\text{diag}} \propto \omega^{-(n_x+1)}$. Specifically, at every iteration of n_x another full particle needs to be moved to or from infinity. For example, even if the number of particles in the system saturates [inset to Fig. 12(c)], application of the same single-particle annihilation operator always meets with a previously relaxed state and hence does not fully destroy the entire state. However, (i) it projects out the part of the state where site k has been occupied, hence this is fully removed from the later dynamics, and (ii) fills site k for the (small) fraction of the previously relaxed state which had no particle at site k . Therefore in any case, as long as the applied operator does not annihilate a given state such that the resulting state can again be normalized, AO applies with integer exponents when creating or annihilating particles without altering the Hamiltonian otherwise.³⁴

The AO exponent that resembles the repeated quantum quenches is only visible at the smallest energies, an energy scale that quickly diminishes to zero with increasing n_x . Therefore eventually the exponent in the low-energy regime is limited by the NRG exponent for a fully thermal distribution at a given finite effective temperature T , i.e. $w_n \propto d^{-n} = (\Lambda^{-n/2})^{2 \log(d)/\log(\Lambda)}$ for $n > n_T$ [see Sec. II C]. This translates into a fully mixed state space for $\omega \ll T$.

In Fig. 13, the NRG discretization parameter $\Lambda = 2.21$ had been chosen such that the thermal distribution w_n^{grand} has the non-integer exponent $2 \log(d)/\log(\Lambda) \simeq 3.5$ for the low-energy tail. Nevertheless, repeated application of a few local operators with integer AO exponents clearly allows to thermalize the system to the corresponding NRG specific thermal exponent. Within the MPS framework, however, this just implies, that the remainder of the system becomes completely randomized, since the grand-canonical exponent simply implies full degeneracy with respect to the rest of the system.

Finally, an overall trend seen in all panels in Fig. 13 is that by repeated applications of local quenches, the maximum of w_n^{diag} shifts towards larger energies with n_x . Clearly, this can be interpreted as heating of the system, and is analyzed in detail by extending Fig. 13(c) to significantly larger n_x , with the results shown in Fig. 14. Panel (a) analyzes the total energy E_{diag} of the system based on the diagonal ensemble as a function of n_x for three exemplary individual stochastic runs by sampling a larger set of excitations $\hat{f}_{k\sigma}^{(\dagger)}$ in k and spin σ according to a given temperature T (see caption of Fig. 14). The energy E_{diag} is plotted in units of E_{grand} , i.e. the total energy of the system obtained from the grand canonical ensemble at temperature $T_{\text{grand}} = T_K$. We also show the ensemble average of E_{diag} over 100 runs, which shows a slow but steady logarithmic increase, as demonstrated by the inset in Fig. 14(a). This shows, indeed, that the system is being heated up by the application of multiple 1-particle excitations. Due to the underlying logarithmic discretization, however, this heating is slowed down

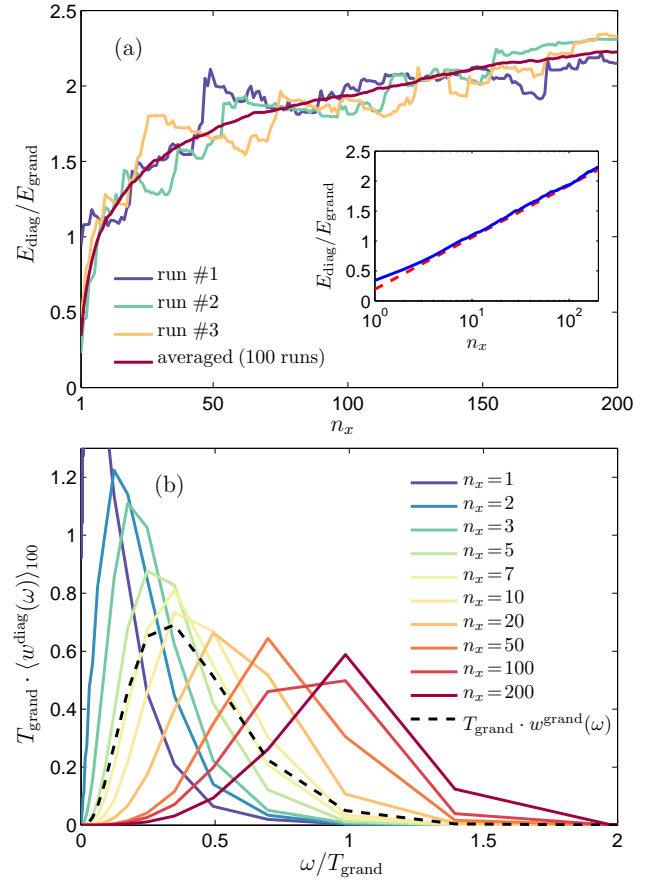


FIG. 14. (color online) (a) Total energy E_{diag} of the system calculated using diagonal ensemble vs. the number of excitations n_x and (b) the weights of the diagonal ensemble w_n^{diag} as a function of energy after having applied n_x single-particle operators, either $\hat{f}_{k\uparrow}^\dagger$ or $\hat{f}_{k\uparrow}$, selected randomly, and applied to shell k with probability $p(k)$ determined by w_n^{grand} . T_{grand} is the temperature used for grand canonical ensemble and E_{grand} is the corresponding energy of the system. In (a) E_{diag} for three exemplary runs is shown together with its ensemble-averaged (over 100 runs) value, which shows a steady logarithmic increase with n_x [inset in (a)]. Panel (b) presents the ensemble-averaged weights $\langle w^{\text{diag}}(\omega) \rangle_{100}$ (over 100 runs) of diagonal density matrix plotted as a function of energy ω with $w^{\text{diag}}(\omega) \equiv w_n^{\text{diag}} \cdot \Lambda^{n/2}$. The dashed line shows the weights of the grand canonical density matrix $w^{\text{grand}}(\omega) \equiv w_n^{\text{grand}} \cdot \Lambda^{n/2}$ as a function of ω .

logarithmically.

The ensemble-averaged weights $\langle w^{\text{diag}}(\omega) \rangle_{100}$ (averaged over 100 runs) of diagonal density matrix are shown in Fig. 14(b) as a function of energy ω on a linear scale, where $w^{\text{diag}}(\omega) \equiv w_n^{\text{diag}} \cdot \Lambda^{n/2}$ [the last factor is justified by the fact that w_n^{diag} represents the integrated weight over an energy interval of width $\propto \Lambda^{-n/2}$]. The dashed line presents the weights of the grand canonical density matrix $w^{\text{grand}}(\omega) \equiv w_n^{\text{grand}} \cdot \Lambda^{n/2}$. Again, one can see that the maximum of $\langle w^{\text{diag}}(\omega) \rangle_{100}$ moves towards larger energies with n_x .

IV. CONCLUSIONS

In this paper we have studied the dynamics of the single-level quantum dot in the Kondo regime, with a special focus on thermalization. The dot was modeled by the single-impurity Anderson Hamiltonian, which was analyzed by the numerical renormalization group. Using the complete eigenbasis of the Hamiltonian obtained by NRG, we calculated the spectral functions of the dot level by using different statistical ensembles. In particular, we determined the spectral function using the grand canonical, microcanonical and diagonal ensembles, which were compared to the spectral function calculated for a state, time-evolved with respect to the full Hamiltonian. The main goal was to test whether the eigenstate thermalization hypothesis also holds for truly many-body systems displaying nontrivial correlations, such as the ones leading to the Kondo effect. The ETH states that, in the long time limit, the system can be described by relatively small number of representative states, as given by the microcanonical ensemble.

We checked the validity of ETH for a few different states of the system, including the ground state, the ground state of decoupled dot, and a few states after having generated an excitation in the bath with either single-particle or density operator. We showed that for initial states where the excitation is created in the bath, the microcanonical ensemble correctly describes the behavior of the system in the long-time limit. Moreover, by calculating the expectation values of the spectral function operator at the Fermi level and the dot occupancy for energy eigenstates relevant for microcanonical ensemble, we showed that the ETH can be indeed invoked to understand the process of thermalization. The eigenstate thermalization hypothesis is thus valid for initial states with an excitation in the bath which, in the NRG context, can be interpreted as macroscopic excitations. However, for states with an excitation in the dot, the long time behavior cannot necessarily be described by a statistical-mechanical ensemble and, as such, the reference to ETH is not meaningful. This mandates an entirely different interpretation in terms of quantum quenches. In particular, when acting locally at the impurity, this essentially leaves the system in its ground state, i.e. at zero temperature. Consequently, it clearly eludes the ETH, and therefore needs to be distinguished from truly thermodynamic statistical ensembles.

ACKNOWLEDGMENTS

This work received support from the DFG (SFB-631, De-730/3-2, De-730/4-2, SFB-TR12). IW acknowledges support from the Alexander von Humboldt Foundation, the EU grant No. CIG-303 689 and the National Science Centre in Poland as the Project No. DEC-2013/10/E/ST3/00213, and AW in addition also DFG Grant WE4819/1-1.

Appendix A: NRG implementation of different ensembles

We study the behavior of an expectation value of observable \hat{O} in the long time limit under the time evolution with respect to the Hamiltonian \hat{H} . The time evolution of a many-body state of the system $|\Psi\rangle$ is given by, $|\Psi_t\rangle = e^{-i\hat{H}t}|\Psi\rangle$. Expanding in the eigenbasis of the Hamiltonian, the time evolution of state $|\Psi\rangle$ becomes,

$$|\Psi_t\rangle \cong \sum_n \sum_{se} e^{-iE_{ns}^D t} C_{nse}^D |se\rangle_n^D, \quad (\text{A1})$$

where the coefficients are defined as $C_{nse}^D \equiv \frac{D}{n} \langle se | \Psi \rangle$. Given an observable \hat{O} , the time evolution of its quantum mechanical expectation value, O_t , is described by

$$O_t = \sum_{nn'} \sum_{se s'e'} e^{i(E_{ns}^D - E_{n's'}^D)t} \times (C_{nse}^D)^* \mathcal{O}_{nse, n's'e'}^{DD} C_{n's'e'}^D, \quad (\text{A2})$$

where $\mathcal{O}_{nse, n's'e'}^{DD} = \frac{D}{n} \langle se | \hat{O} | s'e' \rangle_n^D$ denote the matrix elements of the operator \hat{O} . In general, the evaluation of this expectation value is not trivial, as it includes double sum over the discarded states of the Wilson chain. However, as discussed in App. D [see Eq. (D2)], a double sum over discarded states of the Wilson chain can be converted to a single sum with contributions from both kept and discarded states,^{25,26} and the above formula becomes

$$O_t = \sum_n \sum_{ss'e} \sum_{XX'}^{\neq KK} e^{i(E_{ns}^X - E_{n's'}^X)t} \times (C_{nse}^X)^* \mathcal{O}_{nse, n's'e}^{XX'} C_{n's'e}^{X'}. \quad (\text{A3})$$

In this way a time-dependent expectation value of any observable \hat{O} can be calculated shell-wise in an iterative way by performing a single sweep over the Wilson chain. Note that for more complex operators \hat{O} , such as the spectral function operator \hat{A} , the formula for the expectation value, Eq. (A2), may involve more sums than just two, but it can still be written in a single-sum fashion, with summations over different combinations of matrix elements between kept and discarded states, except for the case when all states are kept, see Eqs. (D3) and (D4).

a. Diagonal ensemble

Equation (A3) implies that the infinite-time average of the observable \hat{O} is given by a *diagonal ensemble*⁷

$$O_{\text{diag}} = \sum_{nse} |C_{nse}^D|^2 \mathcal{O}_{nse, nse}^{DD}, \quad (\text{A4})$$

where the coefficient $|C_{nse}^D|^2$ gives the weight of state $|se\rangle_n^D$ in the ensemble. These coefficients can be used to

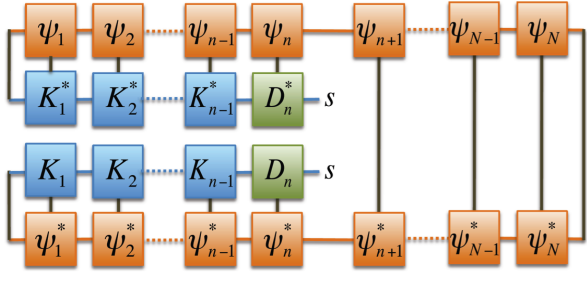


FIG. 15. (color online) MPS representation of the coefficients $\sum_e |C_{nse}^D|^2 = \sum_e \langle \Psi | se \rangle_n^{DD} \langle se | \Psi \rangle$, where the discarded state $|se\rangle_n^D$ is defined graphically in Fig. 1. The kept and discarded blocks are denoted by $X = K$ ($X = D$), respectively, while the corresponding blocks of the state $|\Psi\rangle$ are denoted by ψ_n for shell n . The star denotes complex conjugation.

define a *diagonal* density matrix,

$$\hat{\rho}_{\text{diag}} \equiv \sum_{nse} |C_{nse}^D|^2 |se\rangle_n^{DD} \langle se|. \quad (\text{A5})$$

It can be written in terms of shell-diagonal density matrices, $\hat{\rho}_n^{\text{diag}}$, as

$$\hat{\rho}_{\text{diag}} \equiv \sum_n w_n^{\text{diag}} \hat{\rho}_n^{\text{diag}}, \quad (\text{A6})$$

where $w_n^{\text{diag}} \equiv \sum_{se} |C_{nse}^D|^2$, with $\sum_n w_n^{\text{diag}} = 1$, describes the cumulative weight of shell n to the density matrix $\hat{\rho}_{\text{diag}}$. A diagram for the calculation of the coefficients $|C_{nse}^D|^2$ is shown in Fig. 15. By using Eq. (A4), the expectation value of operator \hat{O} using the diagonal density matrix can be written as

$$O_{\text{diag}} = \sum_n w_n^{\text{diag}} \text{Tr}_{s_n} (\hat{\rho}_n^{\text{diag}} \hat{O}_n), \quad (\text{A7})$$

with $(\mathcal{O}_n)_{ss'} \equiv \langle s | \hat{O} | s' \rangle_n^D$, where Tr_{s_n} denotes the trace over states $s \in D$ at shell n .

b. Microcanonical ensemble

Now, according to the eigenstate thermalization hypothesis,^{5–7} to describe the long time behavior of the system it is sufficient to consider just a number of representative states of appropriate energy, as given by the microcanonical ensemble:

$$O_{\text{micro}} = \frac{1}{N_{\Psi}} \sum_{\substack{nse \\ |E_{ns}^D - E_{\Psi}| \leq \delta E_{\Psi}}} \mathcal{O}_{nse, nse}^{DD}. \quad (\text{A8})$$

Here, E_{Ψ} is the energy of state $|\Psi\rangle$ as in Eq. (3), i.e. relative to the ground state energy $E_0 = \langle \mathcal{G} | \hat{H} | \mathcal{G} \rangle$, with $|\mathcal{G}\rangle$ the full ground state of the system. Furthermore, δE_{Ψ} characterizes the energy fluctuations, and N_{Ψ} is the

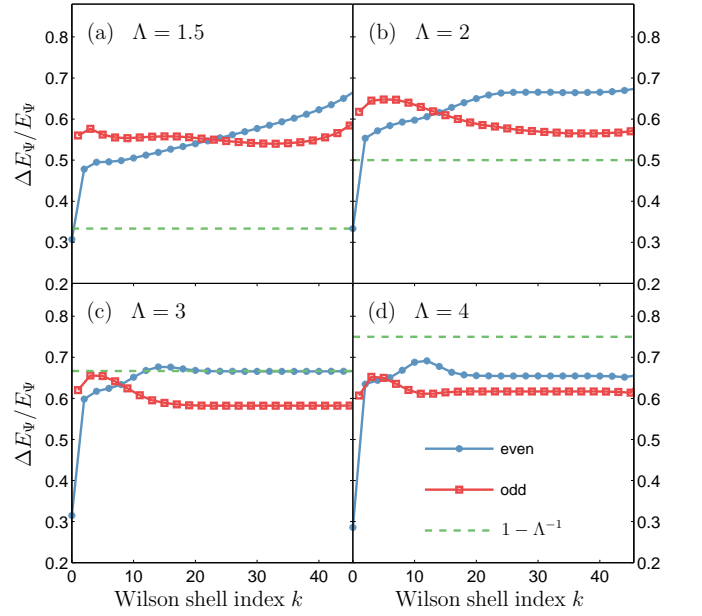


FIG. 16. (color online) The dependence of relative energy uncertainty $\Delta E_{\Psi}/E_{\Psi}$ on Wilson shell index for excited states $|\Psi\rangle = \hat{f}_{k\uparrow}^{\dagger} |\mathcal{G}\rangle$ and for different discretization parameters: (a) $\Lambda = 1.5$, (b) $\Lambda = 2$, (c) $\Lambda = 3$, and (d) $\Lambda = 4$. The horizontal dashed lines indicate the estimate for the relative energy uncertainty, $\delta E_{\Psi}/E_{\Psi} = 1 - \Lambda^{-1}$.

number of energy eigenstates in interval $|E_{ns}^D - E_{\Psi}| \leq \delta E_{\Psi}$.

Regarding the energy uncertainty δE_{Ψ} , however, consider first the relative energy uncertainty $\Delta E_{\Psi}/E_{\Psi}$ as defined in Eq. (3). For excited states of the form $|\Psi\rangle = \hat{f}_{k\uparrow}^{\dagger} |\mathcal{G}\rangle$, this is evaluated and presented in Fig. 16 as a function of the Wilson shell index n , where each panel corresponds to a different discretization parameter Λ , as indicated. Clearly, this needs to be distinguished from $\delta E_{\Psi}/E_{\Psi}$, which determines the energy window that enters the microcanonical expectation value O_{micro} . While for an energy eigenstate one trivially has $\Delta E_{\Psi} = 0$, for a general state $|\Psi\rangle$, $\Delta E_{\Psi}/E_{\Psi} > 0$. As can be seen in Fig. 16, for excited states obtained after acting with a creation operator $\hat{f}_{k\uparrow}^{\dagger}$ on the ground state of the system, $\Delta E_{\Psi}/E_{\Psi}$ is smaller than unity, but clearly finite, and for late iterations reaches $\Delta E_{\Psi}/E_{\Psi} \approx 0.65$, irrespective of discretization parameter Λ [for panel (a) the Wilson shell index is not sufficiently large to resolve the underlying low-energy fixed point, as seen in the later panels; essentially the panels zoom out to reach smaller energy scales for later panels, i.e. with increasing Λ]. However, in the continuum limit, $\Lambda \rightarrow 1^+$, one would expect that $|\Psi\rangle$ in the long time limit behaves similar to an energy eigenstate with energy E_{Ψ} and the energy fluctuations are suppressed, i.e. $\delta E_{\Psi} \ll \Delta E_{\Psi} < E_{\Psi}$. However, due to finite energy resolution when using NRG, it is not possible to take $\delta E_{\Psi} \ll \Delta E_{\Psi}$, since otherwise the energy window for the microcanonical ensemble in Eq. (8) may

contain only very few states or no states at all. Therefore, for the results presented in the main paper, we took the finite energy window for the microcanonical ensemble,

$$\frac{\delta E_\Psi}{E_\Psi} = 1 - \frac{1}{\Lambda}, \quad (\text{A9})$$

which is also indicated by the horizontal dashed lines in Fig. 16. This choice has the correct thermodynamic limit, $\lim_{\Lambda \rightarrow 1^+} (\delta E_\Psi / E_\Psi) = 0^+$. The motivation for Eq. (A9) is given by the underlying logarithmic discretization: if one considers the bath alone and takes an arbitrary state at energy scale E_Ψ , then based on the underlying single-particle energies, one expects an energy resolution in terms of the single-particle level spacing $E_\Psi [1 - \Lambda^{-1}, 1 + \Lambda]$, the minimum of which was used to set δE_Ψ . This choice guarantees that one has a comparable number of representative energy eigenstates within a given energy window. Moreover, with $\delta E_\Psi / E_\Psi$ clearly smaller than 1, only a finite window of Wilson shells of comparable width will contribute to microcanonical ensemble for a given state $|\Psi\rangle$.

For the microcanonical ensemble then one can use the complete NRG eigenbasis to define a *microcanonical* density matrix, $\hat{\rho}_{\text{micro}}$, in the following manner. First, we calculate the energy E_Ψ for state $|\Psi\rangle$. Then, we find all the eigenstates $|se\rangle_n^D$ of energy E_{ns}^D that obey, $|E_{ns}^D - E_\Psi| \leq \delta E_\Psi$, and the shells they belong to, $n = n_1, \dots, n_2$. Let N_n denote the number of such states that contribute for given shell n . Then, the effective total number of contributing states within the NRG is given by, $N_\Psi = \sum_{n=n_1}^{n_2} N_n d^{n_2-n}$, where $d = 4$ is the dimension of the local space and we have also taken into account the degeneracy of the environmental states. We can thus build a normalized *mixed* density matrix for each shell, $\hat{\rho}_n^{\text{micro}}$. Knowing the mixed density matrices, one can construct the full microcanonical density matrix,

$$\hat{\rho}_{\text{micro}} \equiv \sum_n w_n^{\text{micro}} \hat{\rho}_n^{\text{micro}}, \quad (\text{A10})$$

where the weights w_n^{micro} take into account the effect of degeneracies. They are given by $w_n^{\text{micro}} = N_n d^{n_2-n} / Z$, for $n = n_1, \dots, n_2$, and $w_n^{\text{micro}} = 0$ otherwise, with the partition function Z chosen such that $\sum_n w_n^{\text{micro}} = 1$. The microcanonical expectation value, Eq. (A8), can be simply written then as,

$$O_{\text{micro}} = \sum_n w_n^{\text{micro}} \text{Tr}_{s_n} (\hat{\rho}_n^{\text{micro}} \hat{O}_n). \quad (\text{A11})$$

c. Grand canonical ensemble

The grand canonical expectation value O_{grand} can be obtained from

$$O_{\text{grand}} = \sum_n w_n^{\text{grand}} \text{Tr}_{s_n} (\hat{\rho}_n^{\text{grand}} \hat{O}_n), \quad (\text{A12})$$

with the density matrix and corresponding weights as defined in Sec. II C.

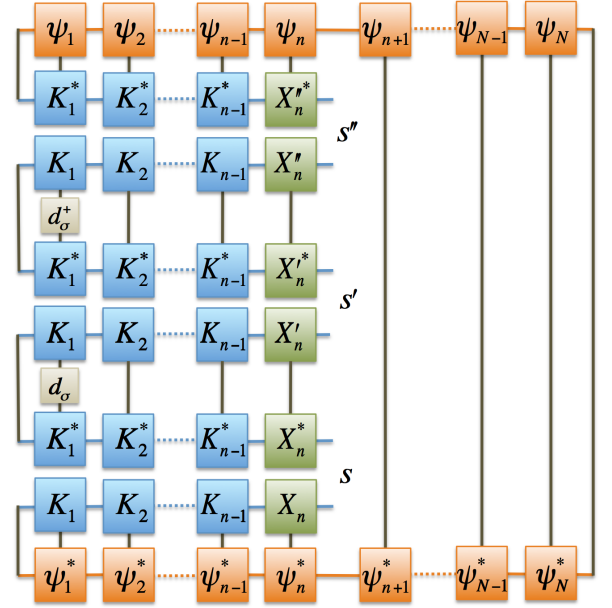


FIG. 17. (color online) MPS representation of a contribution to the time-averaged spectral function of the system due to $\hat{d}_\sigma(t) \hat{d}_\sigma^\dagger(0)$. The open indices need to be summed and multiplied with appropriate exponentials and matrix elements, see Eq. (B2). Summation over shells $n = n_0, \dots, N$ and states $XX'X'' \neq KKK$ also needs to be applied.

Appendix B: Time-averaged spectral function

The time-averaged spectral function can be calculated from Eq. (16), where A_t is explicitly given by [cf. Eq. (A3)]

$$A_t = \sum_{nss'e} \sum_{\neq KKK}^{XX'} e^{i(E_{ns}^X - E_{ns'}^{X'})t} (C_{nse}^X)^* \mathcal{A}_{nse,ns'e}^{XX'} C_{ns'e}^{X'}. \quad (\text{B1})$$

The calculation is not trivial, since it in general involves triple sums over discarded states of the Wilson chain. In particular, a contribution to A_t due to, e.g., $\hat{d}_\sigma(\tau) \hat{d}_\sigma^\dagger(0)$, is explicitly given by

$$A_t^{(1)} = \sum_{nss'e} \sum_{\neq KKK}^{XX'X''} e^{i(E_{ns}^X - E_{ns''}^{X''})t} \delta(\omega + E_{ns}^X - E_{ns'}^{X'}) \times (C_{nse}^X)^* (d_\sigma)_{nse,ns'e}^{XX'} (d_\sigma^\dagger)_{ns'e,ns''e}^{X'X''} C_{ns''e}^{X''}, \quad (\text{B2})$$

the second line of which is illustrated in Fig. 17. Note that in Eq. (B2) we have used the property (D4) to convert the triple sum over discarded states into a single sum over the Wilson chain with contributions coming from all but KKK states. Using Eq. (B2), the corresponding data points can be calculated efficiently in a single-sweep fashion. At given iteration n , one needs to perform all the contractions illustrated in Fig. 17, sum over the combinations of discarded and kept states with $XX'X'' \neq KKK$ while multiplying the open indices with proper exponen-

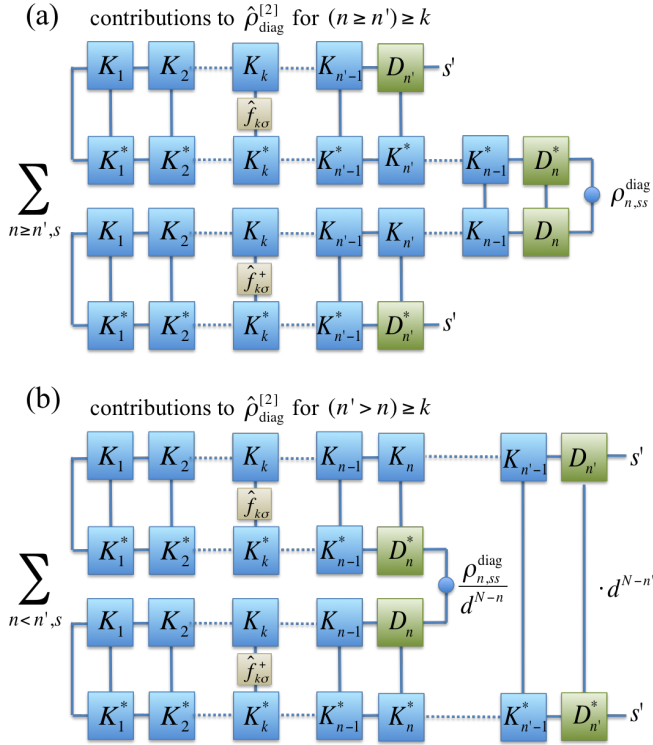


FIG. 18. (color online) MPS representation of contributions to element of the new diagonal density matrix, $\rho_{n',s's'}^{\text{new}}$, see Eqs. (C4) and (C5), after having applied a local operator, $\hat{f}_{k\sigma}^\dagger$, at shell k . Note that consistent tracking of environmental degeneracy leads to the additional factor $d^{N-n'}/d^{N-n} = 1/d^{n-n'}$.

tials, and finally sum up the contributions from all Wilson shells with $n = n_0, \dots, N$. The second contribution, $A_t^{(2)}$, to the time-averaged spectral function A_{time} due to $\hat{d}_\sigma^\dagger(0)\hat{d}_\sigma(\tau)$ has a form similar to Eq. (B2), with $\hat{d}_\sigma \leftrightarrow \hat{d}_\sigma^\dagger$. The time averaging is eventually performed by integrating the phase factors, $\exp[i(E_{ns}^X - E_{ns''}^X)t]$, occurring in Eq. (B2), over time interval $(t_{\text{fin}} - \delta t, t_{\text{fin}})$ and dividing by δt , see Eq. (16). We also note that the calculation of A_Ψ , i.e. for $|\Psi_{t=0}\rangle$, is much simpler than the calculation of A_{time} , since it requires only a double summation over discarded states.

Appendix C: Local operator applied to diagonal density matrix

Consider a density matrix $\hat{\rho}$. Its decomposition over the Wilson shells n will have the contributions $\hat{\rho}_n^{XX'}$, with $XX' \neq KK$. In the long-time limit the off-diagonal matrix elements average out and the density matrix becomes diagonal

$$\hat{\rho}_{\text{diag}} = \sum_{n,s} |s\rangle_n^D \langle s| \cdot \rho_{n,ss}^{\text{diag}}, \quad (\text{C1})$$

with $w_n^{\text{diag}} = \text{Tr}[\hat{\rho}_n^{\text{diag}}]$, and the environment w.r.t. shell n already traced out and included in $\rho_{n,ss}^{\text{diag}}$. By construction of complete basis sets, this density matrix is diagonal in the space of discarded states. Reintroducing the state space for the full Wilson chain including the environmental states e , it can be written as

$$\hat{\rho}_{\text{diag}}^{[1]} = \sum_{nse} |se\rangle_n^D \langle se| \cdot \frac{\rho_{n,ss}^{\text{diag}}}{d^{N-n}}. \quad (\text{C2})$$

Now assume a 1-particle excitation is applied at shell k , say $\hat{f}_{k\sigma}^\dagger$, onto the given density matrix $\hat{\rho}_{\text{diag}}^{[1]}$. This results in a new non-diagonal density matrix

$$\hat{\rho}_{\text{new}} \equiv \hat{f}_{k\sigma}^\dagger \hat{\rho}_{\text{diag}} \hat{f}_{k\sigma}. \quad (\text{C3})$$

Again assuming that in the long-time limit the off-diagonal matrix elements average out, this density matrix can be projected onto its diagonal matrix elements, resulting in the new diagonal density matrix

$$\hat{\rho}_{\text{diag}}^{[2]} = \sum_{n's'e'} |s'e'\rangle_n^D \langle s'e'| \cdot \rho_{n',s's'}^{\text{new}}, \quad (\text{C4})$$

with the diagonal matrix elements

$$\begin{aligned} \rho_{n',s's'}^{\text{new}} &\equiv \sum_{e'} \langle s'e'| \hat{\rho}_{\text{new}} |s'e'\rangle_n^D \\ &= \sum_{nse,e'} \langle s'e'| \hat{f}_{k\sigma}^\dagger |se\rangle_n^D \frac{\rho_{n,ss}^{\text{diag}}}{d^{N-n}} \langle se| \hat{f}_{k\sigma} |s'e'\rangle_n^D. \end{aligned} \quad (\text{C5})$$

This involves two independent summations over Wilson shells, which in the usual spirit of Anders-Schiller (AS) basis^{25,26} can be reduced to a single sum over shells based on energy scale separation (see also App. D). Therefore the new density matrix is defined by its contributions for each shell. The main non-trivial contributions arise from the terms $(n, n') \geq k$, with the contributions $n \geq n'$ ($n < n'$) depicted in Fig. 18, panel (a) and (b), respectively, using the MPS diagrams. Note that in panel (a) the degeneracy factor d^{N-n} in $\hat{\rho}_{\text{diag}}$, see Eq. (C2), again drops out. In contrast, in panel (b) the overall degeneracy factor acquires the correction $d^{n-n'}$. The sum $\sum_{n \geq n'}$ in panel (a) can be computed in a single prior backward sweep, similar to the full-density-matrix (fdm)-NRG spirit.³⁵ Moreover, also the sum $\sum_{n \leq n'}$ in panel (b) can be computed in a single convoluted forward sweep.

In addition, there is one further relevant, yet simple contribution to $\hat{\rho}_{\text{diag}}^{[2]}$ where either n or n' are smaller than k . The only non-zero contribution of this type is $(n = n') < k$,

$$\rho_{n',s's'}^{\text{new}} = \rho_{n',s's'}^{\text{diag}} \cdot \langle \hat{f}_{k\sigma}^\dagger \hat{f}_{k\sigma} \rangle_{T=\infty} = \frac{1}{2} \cdot \rho_{n',s's'}^{\text{diag}}. \quad (\text{C6})$$

This, of course, is only relevant for iterations n' where the initial density matrix had a finite contribution $w_{[1]:n'}^{\text{diag}}$ to start with.

Appendix D: Useful relations

In this appendix we collect some relations that are very useful for explicitly performing (multiple) sums over complete sets of NRG basis states. One such identity is that the sum over discarded eigenstates of shells $n' > n$ is equal to the sum over kept eigenstates of single shell n

$$\sum_{n' > n} \sum_{se} |se\rangle_{n'n'}^{DD} \langle se| = \sum_{se} |se\rangle_n^{KK} \langle se|. \quad (\text{D1})$$

Henceforth, this will be simply abbreviated by writing, $\sum_{n' > n}^D = \sum_{n'=n}^K$. Note that the summation \sum_n^X is the shorthand notation for summing over discarded ($X = D$) or kept ($X = K$) states of a given shell n and summing over the shells. The above identity basically allows one to perform the calculations of various expectation values in a single sweep over the Wilson chain.

The double sum over the discarded states can be then written as^{25,26}

$$\begin{aligned} \sum_{nn'}^{DD} &= \sum_{n=n'}^{DD} + \sum_{n < n'}^{DD} + \sum_{n > n'}^{DD} \\ &= \sum_n^{DD} + \sum_n^{DK} + \sum_n^{KD} = \sum_n^{\neq KK} \sum_{XX'} \end{aligned}, \quad (\text{D2})$$

where this double sum has been split into three terms, the first one with $n = n'$ and the second (third) sum with $n < n'$ ($n > n'$), and then the property (D1) has been exploited.

In a similar way, for triple sum over discarded states we can then write

$$\begin{aligned} \sum_{nn'n''}^{DDD} &= \sum_{n=n'=n''}^{DDD} + \sum_{n < n'=n''}^{DDD} + \sum_{n'=n < n''}^{DDD} + \sum_{n'' < nn'}^{DDD} \\ &+ \sum_{n=n' < n''}^{DDD} + \sum_{n'=n'' < n}^{DDD} + \sum_{n=n'' < n'}^{DDD} \\ &= \sum_n^{DDD} + \sum_n^{DKK} + \sum_n^{KDK} + \sum_n^{KKD} \\ &+ \sum_n^{DDK} + \sum_n^{KDD} + \sum_n^{DKD} \\ &= \sum_n^{\neq KKK} \sum_{XX'X''} \end{aligned}. \quad (\text{D3})$$

Generalizing the above relations, expressions involving M sums over discarded states can be written in the following single-sum form

$$\sum_{n_1 n_2 \dots n_M}^{DD \dots D} = \sum_n^{\neq KKK \dots K} \sum_{X_1 X_2 \dots X_M}. \quad (\text{D4})$$

This formula enables the calculation of various operator expectation values in a single sweep fashion by collecting all the kept-discarded contributions, excluding terms where all the states belong to the kept state space.

* weymann@amu.edu.pl

¹ K. Sengupta, S. Powell, and S. Sachdev, Phys. Rev. A **69**, 053616 (2004).
² J. Berges, S. Borsanyi, and C. Wetterich, Phys. Rev. Lett. **93**, 142002 (2004).
³ N. S. Krylov, *Works on the Foundation of Statistical Physics* (Princeton Univ. Press, Princeton, 1979).
⁴ K. Huang, *Statistical Mechanics* (Wiley, New York, 1987).
⁵ J. M. Deutsch, Phys. Rev. A **43**, 2046 (1991).
⁶ M. Srednicki, Phys. Rev. E **50**, 888 (1994).
⁷ M. Rigol, V. Dunjko, and M. Olshanii, Nature **452**, 854 (2008).
⁸ M. Rigol, Phys. Rev. Lett. **103**, 100403 (2009); Phys. Rev. A **80**, 053607 (2009).
⁹ Amy C. Cassidy, Charles W. Clark, and Marcos Rigol, Phys. Rev. Lett. **106**, 140405 (2011).
¹⁰ Marcos Rigol and Mark Srednicki, Phys. Rev. Lett. **108**, 110601 (2012).
¹¹ Clemens Neuenhahn and Florian Marquardt, Phys. Rev. E **85**, 060101 (2012).
¹² Arnau Riera, Christian Gogolin, and Jens Eisert, Phys. Rev. Lett. **108**, 080402 (2012).
¹³ S. Ziraldo and G. E. Santoro, Phys. Rev. B **87**, 064201 (2013).
¹⁴ K. G. Wilson, Rev. Mod. Phys. **47**, 773 (1975).

¹⁵ R. Bulla, T. A. Costi, and T. Pruschke, Rev. Mod. Phys. **80**, 395 (2008).
¹⁶ P. W. Anderson, Phys. Rev. **124**, 41 (1961).
¹⁷ H. R. Krishna-murthy, J. W. Wilkins, and K. G. Wilson, Phys. Rev. B **21**, 1003 (1980).
¹⁸ Y. Meir and N. S. Wingreen, Phys. Rev. Lett. **68**, 2512 (1992).
¹⁹ Yigal Meir, Ned S. Wingreen, and Patrick A. Lee, Phys. Rev. Lett. **70**, 2601 (1993).
²⁰ J. Kondo, Prog. Theor. Phys. **32**, 37 (1964).
²¹ A. C. Hewson, *The Kondo Problem to Heavy Fermions* (Cambridge University Press, Cambridge, 1993).
²² D. Goldhaber-Gordon, H. Shtrikman, D. Mahalu, D. Abusch-Magder, U. Meirav, and M. A. Kastner, Nature (London) **391**, 156 (1998).
²³ S. Cronenwett, T. H. Oosterkamp, and L. P. Kouwenhoven, Science **281**, 182 (1998).
²⁴ W. G. van der Wiel, S. De Franceschi, T. Fujisawa, J. M. Elzerman, S. Tarucha and L. P. Kouwenhoven, Science **289**, 2105 (2000).
²⁵ F. B. Anders and A. Schiller, Phys. Rev. Lett. **95**, 196801 (2005).
²⁶ F. B. Anders and A. Schiller, Phys. Rev. B **74**, 245113 (2006).
²⁷ A. Weichselbaum and J. von Delft, Phys. Rev. Lett. **99**,

- 076402 (2007).
- ²⁸ R. Peters, T. Pruschke, and F. B. Anders, Phys. Rev. B **74**, 245114 (2006).
- ²⁹ A. Weichselbaum, F. Verstraete, U. Schollwöck, J. I. Cirac, and J. von Delft, Phys. Rev. B **80**, 165117 (2009).
- ³⁰ F. D. M. Haldane, Phys. Rev. Lett. **40**, 416 (1978).
- ³¹ A. Rosch, Eur. Phys. J. B **85**, 6 (2012).
- ³² P. W. Anderson, Phys. Rev. Lett. **18**, 1049 (1967); Phys. Rev. **164**, 352 (1967); K. D. Schotte and U. Schotte, Phys. Rev. **182**, 479 (1969); P. Nozieres, J. Gavoret, and B. Roulet, Phys. Rev. **178**, 1084 (1969).
- ³³ A. Weichselbaum, W. Mündler, and J. von Delft, Phys. Rev. B **84**, **075137** (2011).
- ³⁴ W. Mündler, A. Weichselbaum, M. Goldstein, Y. Gefen, and J. von Delft, Phys. Rev. B **85**, 235104 (2012).
- ³⁵ A. Weichselbaum, Phys. Rev. B **86**, 245124 (2012).